SIAM J. SCI. COMPUT.
Vol. 44, No. 2, pp. B310–B338

PROJECTION METHOD FOR DROPLET DYNAMICS ON GROOVE-TEXTURED SURFACE WITH MERGING AND SPLITTING*

YUAN GAO† AND JIAN-GUO LIU‡

Abstract. The geometric motion of small droplets placed on an impermeable textured substrate is mainly driven by the capillary effect, the competition among surface tensions of three phases at the moving contact lines, and the impermeable substrate obstacle. After introducing an infinite dimensional manifold with an admissible tangent space on the boundary of the manifold, by Onsager's principle for an obstacle problem, we derive the associated parabolic variational inequalities. These variational inequalities can be used to compute the contact line dynamics with unavoidable merging and splitting of droplets due to the impermeable obstacle. To efficiently solve the parabolic variational inequality, we propose an unconditional stable explicit boundary updating scheme coupled with a projection method. The explicit boundary updating efficiently decouples the computation of the motion by mean curvature of the capillary surface and the moving contact lines. Meanwhile, the projection step efficiently splits the difficulties brought by the obstacle and the motion by mean curvature of the capillary surface. Furthermore, we prove the unconditional stability of the scheme and present an accuracy check. Convergence of the proposed scheme is also proved using a nonlinear Trotter–Kato product formula under the pinning contact line assumption. After incorporating the phase transition information at splitting points, several challenging examples including splitting and merging of droplets are demonstrated.

Key words. free boundary, obstacle problem, variational inequality, mean curvature flow, moving contact line, Onsager principle

AMS subject classifications. 35R35, 35K93, 35K86, 65K15, 74A50

DOI. 10.1137/20M1338563

1. Introduction.

The contact line dynamics for droplets placed on an impermeable groove-textured substrate is a historical and challenging problem. The capillary effect caused by the interfacial energy dominates the dynamics of small droplets, because the ratio between the surface area and the bulk volume is large. The capillary effect is particularly important to the moving contact lines, where three phases (liquid, solid, gas) meet. For small droplets with capillary effect, the geometric dynamics is essentially a mean curvature flow for the capillary surface (the interface between fluids inside the droplet and gas surrounding the droplet) associated with free boundaries (moving contact lines) on the impermeable groove-textured substrate. The mechanics for the contact line dynamics is determined by Onsager's linear response relation between contact line speed v_{CL} and the unbalanced Young force F_Y; see (2.17). The dynamic contact angle θ_{CL} then tends to relax to the equilibrium contact angle (i.e., Young's angle θ_Y) which is determined by the competitions among the surface tensions of three interfaces at the contact lines; see (2.5).

The dynamics become more complicated after considering a nonlocal volume preserving constraint, a groove-textured substrate with constantly changed slopes,

*Submitted to the journal's Computational Methods in Science and Engineering section May 18, 2020; accepted for publication (in revised form) October 21, 2021; published electronically March 21, 2022.

https://doi.org/10.1137/20M1338563

Funding: The work of the second author was supported by the National Science Foundation under grants DMS-1812573 and DMS-210698.

†Department of Mathematics, Purdue University, West Lafayette, IN 47906 USA (gao662@purdue.edu).

‡Department of Mathematics and Department of Physics, Duke University, Durham, NC 27708 USA (jliu@phy.duke.edu).

a gravitational effect, and unavoidable topological changes such as splitting and merging due to the impermeable groove-textured substrate. In this paper, we focus on variational derivations, numerical methods, and stability/convergence analysis for this challenging obstacle problem coupled with the droplet dynamics, which consist of (i) an obstacle-type weak formulation of the motion by mean curvature for the capillary surface and (ii) the moving contact line boundary conditions.

On the one hand, for a pure mean curvature flow model with an obstacle but without contact line dynamics, we refer to [1, 33] for local existence and uniqueness of a regular solution by constructing a minimizing movement sequence. On the other hand, for the moving contact line boundary condition coupled with the quasi-static dynamics for the capillary surface, there are some analysis results on global existence and homogenization problems; see [6, 23, 26, 17] for the capillary surface described by a harmonic equation and see [7, 8, 9, 18] for the capillary surface described by a spatial-constant mean curvature equation. Particularly, using a minimizing movement method with a set-distance as a dissipation functional, [17] constructed a unique global solution starting from a star-shaped initial wetting domain but under a quasi-static assumption for the capillary surface and with a Dirichlet energy instead of an interfacial energy. This construction for the free boundary problem was first developed in [2] and [32] independently, which are indeed the original works giving rise to the lately developed minimizing movement method for general problems.

However, the contact line dynamics for droplets with an unavoidable topological change including splitting and merging due to an impermeable obstacle are lack of study in terms of both variational derivations, mathematical analysis, and efficient algorithms. Particularly, the original minimizing movement discretization for the mean curvature flow uses a set-distance, which is very hard to implement numerically. It is even more complicated to implement for obstacle problems with moving contact lines and splitting phenomena.

First, we will regard the full dynamics of a droplet with moving contact lines and an impermeable obstacle substrate as a curve on an infinite dimensional manifold $\mathcal{M}$ with a boundary; see section 2.2.1. Then after introducing a free energy $\mathcal{F}$, an admissible tangent space $T\mathcal{M}$, and a Rayleigh dissipation functional Q, by using Onsager's principle for an obstacle problem, we derive two parabolic variational inequalities (PVIs); see PVI (2.26) for a virtual velocity formulation and see PVI (2.29) for a virtual displacement formulation. PVI (2.29) is derived by minimizing a Rayleighian in a subset of the admissible tangent space; however, it is computationally friendly and we will prove that these two versions of PVIs are equivalent and have the same strong formulation (see Proposition 2.1).

Second, after including a textured substrate, for PVI (3.31), we propose a numerical scheme based on an unconditionally stable explicit updating for moving contact lines and a projection method for the obstacle problem; see section 3.1. The explicit boundary updating efficiently decouples the computations for the moving contact line and the motion of the capillary surface. Meanwhile, the projection operator for the mean curvature flow of droplets with volume constraint has a closed formula characterization (see (1.4) and Lemma 3.2), so the proposed numerical scheme based on the projection method (splitting method) is very efficient and easy to implement. Unconditional stability of the projection method is proved in Proposition 3.1, which focuses on the difficulties brought by the moving contact line, and the motion by mean curvature with an obstacle. We also find the pure PVI formulation misses the phase transition information at splitting (merging) points where the interface between two phases becomes an emerged triple junction of three phases, so pure PVI is not

enough to correctly show the physical phenomena. Therefore, we enforce the phase transition and contact line mechanism at emerged triple junctions in the last step of the projection method to incorporate both the obstacle information and the phase transition information at splitting points; see section 3.1.

Next, we provide an analytic validation for the proposed projection method above. Notice that after the explicit boundary updating step, the problem is reduced to finding an efficient implementation of a minimizing movement for a pinning contact line case. In this case, the full dynamics of droplets with an obstacle and volume constraint can be formulated as a gradient flow of the sum of two convex functionals $\mathcal{F}+I_K$ in a Hilbert space. More precisely, let K be a closed convex subset in a Hilbert space X_1; see specific definition (3.32) and (3.37) in section 3.3.2 after including the volume constraint. Thus using an indicator functional $I_K(u) := \begin{cases} 0, & u \in K; \\ +\infty, & u \notin K, \end{cases}$ to seek solution $u(t) \in K$ of PVI (3.31) is equivalent to seeking the unique mild solution [5] in X_1 generated by the sum of two maximal monotone operators $\nabla\mathcal{F} + \partial I_K$, i.e.,

$$\partial_t u(t) \in -(\nabla\mathcal{F} + \partial I_K)(u(t)) \quad \text{for a.e. } t > 0,\ u(0) = u_0. \tag{1.1}$$

Notice here we already take advantage of the efficient local information from Gâteaux derivative $\nabla\mathcal{F}$ instead of using the subdifferential $\partial\mathcal{F}$. Then the standard minimizing movement scheme (backward Euler scheme) is given by the resovent representation

$$u^{k+1} = (I + \tau(\nabla\mathcal{F} + \partial I_K))^{-1}\, u^k. \tag{1.2}$$

Inspired by a nonlinear version of the Trotter–Kato product formula [25] in Hilbert space X_1, the resovent can be approximated by

$$u^{k+1} = (I + \tau\partial I_K)^{-1}(I + \tau\nabla\mathcal{F})^{-1}u^k. \tag{1.3}$$

In Lemma 3.2, for a given reference capillary profile u^* satisfying impermeable obstacle condition $u^* \geq 0$ and the volume constraint $\int u^* \equiv V$, we give the resolvent characterization for the projection operator $\mathrm{Proj}_K(\tilde{u}^{k+1} - u^*)$ in X_1,

$$u^{k+1} = u^* + (I + \tau\partial I_K)^{-1}(\tilde{u}^{k+1} - u^*) \Longleftrightarrow \begin{cases} u^{k+1} = \max\{\tilde{u}^{k+1} + \lambda,\, 0\}, \\ \int_D u^{k+1}\,\mathrm{d}x\,\mathrm{d}y = V, \end{cases} \tag{1.4}$$

which can be easily implemented. Hence in Theorem 3.3, based on the alternate resolvent reformulation (1.3) of our projection method, we apply the Trotter–Kato product formula [25] to finally prove convergence of the projection method in X_1. The spirit of the projection method is same as the one for other efficient splitting methods when solving some important physical problems such as the incompressive Navier–Stokes equation [10, 40] and the Landau–Lifshitz equation [14].

Finally, in section 4, we use a projected triple Gaussian as an initial droplet profile to check the order of convergence of the proposed projection method. The moving contact line, the capillary surface, and the dynamic contact angle all have a perfect first order accuracy. Then several numerical simulations are conducted including the splitting of one droplet on an inclined groove-textured substrate and the merging of two droplets in a Utah teapot.

There are also many other numerical methods for computing the geometric motion of droplets with moving contact lines or for general geometric equations with an obstacle; cf. [30, 34, 47, 16, 15, 44, 45, 42, 3] and the references therein. Particularly,

we compare with those closely related to the geometric motion of droplets with moving contact lines and an impermeable obstacle. The mean curvature flow with obstacles is theoretically studied in [1] in terms of a weak solution constructed by a minimizing movement (implicit time-discretization). The L^2 penalty method for the obstacle problem is introduced in [21, 39], and recently an advanced L^1 penalty method was introduced in [41, 48]. They replace the indicator functional $I_K(u)$ in the total energy by an L^2 (resp., L^1) penalty $\mu\|(g-u)_+\|_{L^2}$ (resp., $\mu\|(w-u)_+\|_{L^1}$) with a large enough parameter μ. The threshold dynamics method based on characteristic functions is first used in [45, 42] to simulate the contact line dynamics, which is particularly efficient and can be easily adapted to droplets with topological changes. The authors extended the original threshold dynamics method for mean curvature flows to the case with a solid substrate and a free energy with multiphase surface tensions, in the form of obstacle problems. However, since they do not enforce the contact line mechanism [11, 37], i.e., the relation between the contact line speed and the unbalanced Young force $v_{\mathrm{CL}} = \frac{\gamma_{\mathrm{LG}}}{\xi}(\cos\theta_Y - \cos\theta_{\mathrm{CL}})$, their computations on the moving contact line and the dynamic contact angles are different with the present paper and only the equilibrium Young angle θ_Y is accurately recovered. Instead, the contact line mechanism in [24, 43] is accurately recovered at each time step. With some local treatments at splitting points, the authors simulate the pinch-off due to an impermeable substrate of solid drops described by the surface diffusion with either a sharp interface dynamics or a corresponding phase field model; see [36] for including hydrodynamic effects. We point out the explicit front tracking method based on Lagrangian coordinates in [43] is convenient for simulation of the pinch-off. However, the Courant–Friedrichs–Lewy condition constraint for this explicit method is severe. Besides, the level-set method developed in [31, 44] cannot be directly used and also cannot deal with textured substrates which lead to PVIs for obstacle problems. For other general geometric equations including the motion by mean curvature for a two-phase flow model, we refer to a review article [3] and references therein for a parametric finite element method, which is particularly useful for high dimensional problems.

The remaining part of the paper will be organized as follows. In section 2, we derive the associated PVIs for the contact line dynamics by Onsager's principle for an obstacle problem. In section 3, we propose an unconditionally stable explicit boundary updating scheme coupled with the projection method for solving PVI and the phase transition information for merging and splitting. The stability and convergence analysis are given in sections 3.2 and 3.3. In section 4, we give an accuracy check for the projection method and conduct several computations including merging and splitting of droplets on groove-textured substrate.

2. Parabolic variational inequalities of droplet dynamics derived by Onsager's principle with an obstacle. In this section, we derive PVIs for the contact line dynamics with an impermeable substrate as an obstacle. We first introduce the configuration state (the contact domain and the capillary surface) and the free energy of the contact line dynamics. Then we regard the configuration space as an infinite dimensional manifold with a boundary and give kinematic descriptions for the full dynamics including admissible velocities and the first variation of the free energy on the manifold; see sections 2.1 and 2.2. Next, after introducing a Rayleigh dissipation functional, we derive a model for the droplet dynamics with obstacle by energy considerations. We apply Onsager's principle for the obstacle problem to derive two associated PVIs, which can be used to describe the droplet dynamics on a rough substrate with unavoidable merging and splitting; see section 2.3. Finally, we

show the equivalence between two versions of PVIs in Proposition 2.1, one of which will be used to design efficient numerical schemes for the contact line dynamics with an impermeable obstacle.

2.1. Configuration states, free energy, and kinematic description for velocities. We study the motion of a three-dimensional (3D) droplet placed on an impermeable substrate $\{(x, y, z); z = 0\}$. Let the wetting domain (a.k.a. the contact domain) be $(x, y) \in D \subset \mathbb{R}^2$ with boundary $\Gamma := \partial D$ (physically known as the contact lines). We focus on the case that the capillary surface S (the interface between the liquid and the gas) of the droplet is described by a graph function $u(x, y)$. The droplet domain is then identified by the area

$$A := \{(x, y, z);\ (x, y) \in D,\ 0 < z < u(x, y), u|_\Gamma = 0\}$$

with sharp interface $S := \{(x, y, u(x, y)), (x, y) \in D\}$. We will give a kinematic description and a driven energy in this section.

2.1.1. Configuration state, geometric quantities, and kinematic description for velocities of a droplet. First, from the wetting domain and the capillary surface defined above, a configuration state of a droplet is chosen to be (Γ, u) with $u|_\Gamma = 0$.

Second, given a configuration state (Γ, u) with $u|_\Gamma = 0$, we clarify the following geometric quantities; see Figure 1(a). The unit outer normal on the capillary surface is $n := \frac{1}{\sqrt{1+|\nabla u|^2}}(-\nabla u, 1)$. The unit outer normal at the contact line Γ is $n_{\text{CL}} := \frac{-\nabla u}{|\nabla u|}|_\Gamma$, which in three-dimensions is extended as $(n_{\text{CL}}, 0)$. Define the contact angles (inside the droplet A) as θ_{CL} satisfying

$$\sin\theta_{\text{CL}} = n \cdot (n_{\text{CL}}, 0) = \frac{|\nabla u|}{\sqrt{1 + |\nabla u|^2}}, \tag{2.1}$$

which implies $\tan\theta_{\text{CL}} = |\nabla u|$ at Γ.

Third, given a configuration state (Γ, u) with $u|_\Gamma = 0$, we describe two velocities of the droplet and their relations. (i) The motion of contact line Γ in the outer normal direction n_{CL} is described by the contact line speed v_{CL}. (ii) The motion of the capillary surface along the outer normal n is described by the normal speed $v_n = \frac{\partial_t u}{\sqrt{1+|\nabla u|^2}}$. Here $\partial_t u$ is the vertical velocity of the capillary surface, which is convenient to use in the graph representation. (iii) The continuity equation $u(\Gamma(t), t) \equiv 0$ gives the relation between $\partial_t u|_\Gamma$ and v_{CL}.

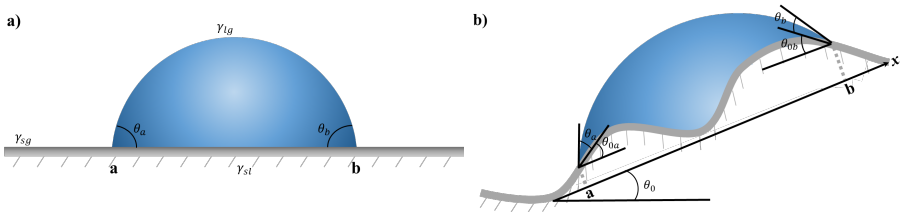

FIG. 1. *Droplets with contact angles θ_a, θ_b and surface tensions $\gamma_{LG}, \gamma_{SG}, \gamma_{SL}$.* (a) *Droplet placed on $z = 0$.* (b) *Droplet placed on an inclined groove-textured surface with effective angle θ_0.*

(2.2)
$$\begin{aligned}\frac{\mathrm{d}u(\Gamma(t),t)}{\mathrm{d}t} &= \partial_t u(\Gamma(t),t) + \nabla u(\Gamma(t),t)\cdot\partial_t\Gamma = \partial_t u(\Gamma(t),t) + (\nabla u(\Gamma(t),t)\cdot n_{\mathrm{CL}})v_{\mathrm{CL}}\\ &= \partial_t u(\Gamma(t),t) - |\nabla u(\Gamma(t),t)|v_{\mathrm{CL}} = 0,\end{aligned}$$

where we used the fact that $n_{\mathrm{CL}} := \frac{-\nabla u}{|\nabla u|}|_\Gamma$.

An important case is to assume the volume preserving constraint $\int_{D(t)} u(x,y,t)\,\mathrm{d}x\,\mathrm{d}y = V$. In this case, by $u(x,y,t) = 0$ on $\Gamma(t)$ and the Reynolds transport theorem, we have

$$\int_{D(t)} \partial_t u\,\mathrm{d}x\,\mathrm{d}y = \frac{\mathrm{d}}{\mathrm{d}t}\int_{D(t)} u(x,y,t)\,\mathrm{d}x\,\mathrm{d}y = 0, \tag{2.3}$$

which gives an additional constraint on the vertical velocity.

2.1.2. Free energy for the droplet and Young's angle. Now we clarify the free energy of a droplet following the notation and terminologies in the classical book of De Gennes, Brochard-Wyart, and Quéré [12]. For a droplet placed on a substrate, the surface tension contributes the leading effect to the dynamics and the equilibrium of the droplet. Especially, for contact line Γ, where three phases of materials (gas, liquid, and solid) meet, one should consider the interactions between their surface energies. Denote $\gamma_{\mathrm{SL}} > 0$ ($\gamma_{\mathrm{SG}}, \gamma_{\mathrm{LG}}$, resp.) as the interfacial surface energy density (a.k.a. surface tension coefficients) between solid-liquid phases (solid-gas, liquid-gas, resp.). To measure the total area of the capillary surface with surface tension γ_{LG} and the area of the contact domain with the relative surface tension $\gamma_{\mathrm{SL}} - \gamma_{\mathrm{SG}}$, we take the total free energy of the droplet as the summation of the surface energy and the gravitational energy

$$\begin{aligned}\mathcal{F} &= \gamma_{\mathrm{LG}}\int_{\partial A(t)\cap\{u>0\}} \mathrm{d}s + (\gamma_{\mathrm{SL}} - \gamma_{\mathrm{SG}})\int_{D(t)} \mathrm{d}x\,\mathrm{d}y + \rho g\int_{D(t)} \frac{u^2}{2}\,\mathrm{d}x\,\mathrm{d}y\\ &= \gamma_{\mathrm{LG}}\int_{D(t)} \sqrt{1+|\nabla u|^2}\,\mathrm{d}x\,\mathrm{d}y + (\gamma_{\mathrm{SL}} - \gamma_{\mathrm{SG}})\int_{D(t)} \mathrm{d}x\,\mathrm{d}y + \rho g\int_{D(t)} \frac{u^2}{2}\,\mathrm{d}x\,\mathrm{d}y,\end{aligned} \tag{2.4}$$

where ρ is the density of the liquid and g is the gravitational acceleration. Besides gravity, we neglect other forces, such as the inertia effect, viscosity stress inside the droplet, the Marangoni effect, electromagnetic fields, evaporation and condensation, etc.

With a fixed volume V, competitions between the three surface tensions will determine uniquely the steady state of the droplet, i.e., the minimizer of $\mathcal{F}$. Define σ as the relative adhesion coefficient between the liquid and the solid,

$$\sigma := \frac{\gamma_{\mathrm{SL}} - \gamma_{\mathrm{SG}}}{\gamma_{\mathrm{LG}}}.$$

We remark that the spreading parameter $S := \gamma_{\mathrm{LG}}(\frac{\gamma_{\mathrm{SG}}-\gamma_{\mathrm{SL}}}{\gamma_{\mathrm{LG}}} - 1)$ could be positive in the so-called total wetting regime [11, section 1.2.1]. But in the current contact angle dynamics setup, $|\sigma| < 1$. By Young's equation [46], the equilibrium contact angle θ_Y is determined by the Young's angle condition

$$\cos\theta_Y = \frac{\gamma_{\mathrm{SG}} - \gamma_{\mathrm{SL}}}{\gamma_{\mathrm{LG}}} = -\sigma. \tag{2.5}$$

We will only focus on the partially wetting (hydrophilic) case $-1 < \sigma < 0$, or equivalently $0 < \theta_Y < \frac{\pi}{2}$. In this case, adhesive forces between the liquid and the solid tend

to spread the droplet across the surface and there is a vertical graph representation of the capillary surface. We refer to [19] for more discussions on dewetting or nonwetting droplets (i.e., $0 < \sigma < 1$) with a horizontal graph representation for the quasi-static case.

2.2. Configuration space as a manifold and the kinematic description for the rate of change of free energy. With the specific driven energy $\mathcal{F}$, we compute the first variation of the free energy for any given virtual displacement. Before that, we first clarify the configuration space as a manifold and define the tangent plane at each point on the manifold.

2.2.1. Configuration space for the obstacle problem: A manifold with a boundary. Here we first give a derivation by taking a flat impermeable substrate $z = 0$ for simplicity. We use an infinite dimensional manifold [28] to describe the configuration space

$$\mathcal{M} := \{(\Gamma, u);\ \Gamma \in C^1,\ u \in C^2(D) \cap L^2(D),\ u \geq 0 \text{ on } D,\ u|_\Gamma = 0\}. \tag{2.6}$$

The dynamics of the droplet is represented by a trajectory on this manifold. Consider a trajectory $\eta(t) \in \mathcal{M}$ starting from initial state $\eta(0) = \{\Gamma(0), u(x, y, 0)\} \in \mathcal{M}$,

$$\eta(t) = \{\Gamma(t), u(x, y, t)\} \in \mathcal{M}, \quad t \in [0, T]. \tag{2.7}$$

2.2.2. Obstacle constraint in the tangent plane: A convex closed subset. Given a configuration state $\eta = \{\Gamma, u\}$, now we use the vertical velocity $v = \partial_t u$ and the contact line speed v_{CL} to describe the tangent plane $T_\eta\mathcal{M}$. To maintain the continuity at the contact line, these two velocities in the tangent plane satisfy the linear restriction (2.2).

Since the geometric motion has an obstacle condition $u \geq 0$, define the coincidence set as

$$B_\eta := \{(x, y) \in D; u(x, y) = 0\}, \tag{2.8}$$

which is a closed subset of D. Manifold $\mathcal{M}$ has a boundary, i.e., $\{\eta \in \mathcal{M}; B_\eta \neq \emptyset\}$. If $B_\eta \neq \emptyset$, then η is on the boundary of the manifold $\mathcal{M}$. In other words, the capillary surface u touches the obstacle on the coincidence set, which will lead to a PVI as described below in section 2.3.

Given $\eta = \{\Gamma, u\}$, define the weighted L^2 space as the ambient space

$$X_\eta := L^2\left(\Gamma \times D;\ \mathrm{d}s \times \frac{1}{\sqrt{1 + |\nabla u|^2}}\,\mathrm{d}x\,\mathrm{d}y\right) \tag{2.9}$$

with the weighted inner product

$$\langle q_1, q_2\rangle_{X_\eta} := \xi \int_\Gamma v_{\text{CL}1} v_{\text{CL}2}\,\mathrm{d}s + \zeta \int_D v_1 v_2 \frac{\mathrm{d}x\,\mathrm{d}y}{\sqrt{1 + |\nabla u|^2}} \tag{2.10}$$

for any $q_1 = (v_{\text{CL}1}, v_1)$, $q_2 = (v_{\text{CL}2}, v_2) \in X_\eta$. Here the constants ξ and ζ are indeed the friction coefficients, which will be explained later.

Then the tangent plane

$$T_\eta\mathcal{M} := \{(v_{\text{CL}}, v) \in C^1(\Gamma \times D);\ v - v_{\text{CL}}|\nabla u|_\Gamma = 0, \quad v \geq 0 \text{ on } B_\eta\} \subset X_\eta \tag{2.11}$$

is a closed convex cone and is embedded in the ambient space X_η with the same inner product as X_η. We remark the last inequality for $T_\eta\mathcal{M}$ in (2.11) becomes effective when η sits on the boundary of the manifold $\mathcal{M}$, i.e., $B_\eta \neq \emptyset$. If $B_\eta = \emptyset$, then the tangent plane $T_\eta\mathcal{M}$ is a linear subspace of X_η.

2.2.3. First variation of the free energy. For an arbitrary trajectory $\tilde{\eta}(s) = \{\tilde{\Gamma}(s), \tilde{u}(x, y, s)\}$ (a.k.a. virtual displacement) starting from $\tilde{\eta}(t) = \eta(t)$ at the tangent direction

$$\tilde{\eta}'(t) = \{\partial_t \tilde{\Gamma}(t), \partial_t \tilde{u}\} = \{\tilde{v}_{\mathrm{CL}} n_{\mathrm{CL}}, \tilde{v}\}, \quad \{\tilde{v}_{\mathrm{CL}}, \tilde{v}\} \in T_{\eta(t)}\mathcal{M}, \tag{2.12}$$

from (2.11) we know

$$\tilde{v}|_{\Gamma(t)} = |\nabla u(\Gamma(t), t)| \tilde{v}_{\mathrm{CL}}. \tag{2.13}$$

To ensure the volume preserving condition $\int_{D(t)} u \,\mathrm{d}x \,\mathrm{d}y = V$, $t \in [0, T]$, we calculate the first variation of an extended free energy $\mathcal{F}(\eta, \lambda)$ on manifold $\mathcal{M} \times \mathbb{R}$ for $\eta(t) \in \mathcal{M}$ and a Lagrange multiplier $\lambda(t)$

$$\mathcal{F}(\eta(t), \lambda(t)) = \mathcal{F}(\eta(t)) - \lambda(t) \left(\int_{D(t)} u(\cdot, t) \,\mathrm{d}x \,\mathrm{d}y - V \right). \tag{2.14}$$

Then we have

$$\begin{aligned} &\frac{\mathrm{d}}{\mathrm{d}s}\Big|_{s=t^+} \mathcal{F}(\tilde{\eta}(s), \tilde{\lambda}(s)) \\ &\quad = \frac{\mathrm{d}}{\mathrm{d}s}\Big|_{s=t^+} \mathcal{F}(\tilde{\eta}(t)) - \frac{\mathrm{d}}{\mathrm{d}s}\Big|_{s=t^+} \tilde{\lambda}(s) \left(\int_{\tilde{D}(s)} \tilde{u}(s) \,\mathrm{d}x \,\mathrm{d}y - V \right) \\ &\quad = \frac{\mathrm{d}}{\mathrm{d}s}\Big|_{s=t^+} \mathcal{F}(\tilde{\eta}(s)) - \lambda(t) \int_{D(t)} \tilde{v} \,\mathrm{d}x \,\mathrm{d}y - \tilde{\lambda}'(t) \left(\int_{D(t)} u \,\mathrm{d}x \,\mathrm{d}y - V \right), \end{aligned} \tag{2.15}$$

where we used (2.12) and the Reynolds transport (2.3) in the last equality.

Now we calculate the first variation for a generic $\mathcal{F}(\tilde{\eta}(s))$ with the energy density function $G(u, \nabla u)$. From (2.13) and the Reynolds transport theorem, we have

$$\begin{aligned} &\frac{\mathrm{d}}{\mathrm{d}s}\Big|_{s=t^+} \int_{\tilde{D}(t)} G(\tilde{u}(x, y, s), \nabla \tilde{u}(x, y, s)) \,\mathrm{d}x \,\mathrm{d}y \\ &\quad = \int_{\Gamma(t)} G|_{\Gamma} \tilde{v}_{\mathrm{CL}} \,\mathrm{d}s + \int_{D(t)} \partial_u G \tilde{v} + \partial_{\nabla u} G \cdot \nabla \tilde{v} \,\mathrm{d}x \,\mathrm{d}y \\ &\quad = \int_{\Gamma(t)} G|_{\Gamma} \tilde{v}_{\mathrm{CL}} \,\mathrm{d}s + \int_{D(t)} (\partial_u G - \nabla \cdot (\partial_{\nabla u} G)) \tilde{v} \,\mathrm{d}x \,\mathrm{d}y + \int_{\Gamma(t)} \tilde{v} (n_{\mathrm{CL}} \cdot \partial_{\nabla u} G) \,\mathrm{d}s \\ &\quad = \int_{\Gamma(t)} [G + |\nabla u| (n_{\mathrm{CL}} \cdot \partial_{\nabla u} G)]\big|_{\Gamma} \tilde{v}_{\mathrm{CL}} \,\mathrm{d}s + \int_{D(t)} (\partial_u G - \nabla \cdot (\partial_{\nabla u} G)) \tilde{v} \,\mathrm{d}x \,\mathrm{d}y. \end{aligned} \tag{2.16}$$

Regard the contact line Γ and the capillary surface S as an open system. Denote the two forces exerted by the droplet (the open system Γ and S) on the environment as

$$F := -\partial_u G + \nabla \cdot (\partial_{\nabla u} G), \quad F_Y := -G - |\nabla u| (n_{\mathrm{CL}} \cdot \partial_{\nabla u} G). \tag{2.17}$$

Then free energy dissipation can be expressed as the virtual work per unit time done by the two virtual forces on the environment. For the case that $G = \gamma_{\mathrm{LG}} \sqrt{1 + |\nabla u|^2} + (\gamma_{\mathrm{SL}} - \gamma_{\mathrm{SG}}) + \rho g \frac{u^2}{2} - \lambda u$, we know

$$F = -\rho g u + \gamma_{\mathrm{LG}} \nabla \cdot \left(\frac{\nabla u}{\sqrt{1 + |\nabla u|^2}} \right) + \lambda = -\rho g u - \gamma_{\mathrm{LG}} H + \lambda, \quad F_Y = \gamma_{\mathrm{LG}} (\cos \theta_{\mathrm{CL}} - \cos \theta_Y), \tag{2.18}$$

where $H = -\nabla \cdot (\frac{\nabla u}{\sqrt{1+|\nabla u|^2}})$ is the mean curvature. In this paper, we choose the convention for the mean curvature notation H so that the sphere with radius R in three dimensions has mean curvature $H = \frac{2}{R}$.

With these two unbalanced forces F, F_Y, we know

$$\begin{aligned} &\frac{\mathrm{d}}{\mathrm{d}s}\Big|_{s=t^+} \mathcal{F}(\tilde{\eta}(s), \tilde{\lambda}(s)) \\ &= -\int_{\Gamma(t)} F_Y \tilde{v}_{\mathrm{CL}} \,\mathrm{d}s - \int_{D(t)} F\tilde{v} \,\mathrm{d}x\,\mathrm{d}y - \tilde{\lambda}'(t)\left(\int_{D(t)} u \,\mathrm{d}x\,\mathrm{d}y - V\right) \end{aligned} \tag{2.19}$$

is a linear functional in terms of $(\tilde{v}_{\mathrm{CL}}, \tilde{v}, \tilde{\lambda}')$. Then after imposing the volume constraint $\int_{D(t)} u \,\mathrm{d}x\,\mathrm{d}y = V$, the energy dissipation is given by

$$\frac{\mathrm{d}}{\mathrm{d}s}\Big|_{s=t^+} \mathcal{F}(\tilde{\eta}(s), \tilde{\lambda}(s)) = -\int_{\Gamma(t)} F_Y \tilde{v}_{\mathrm{CL}} \,\mathrm{d}s - \int_{D(t)} F\tilde{v} \,\mathrm{d}x\,\mathrm{d}y =: \dot{\mathcal{F}}((\tilde{v}_{\mathrm{CL}}, \tilde{v}); \eta). \tag{2.20}$$

We will see below, since the Rayleigh dissipation functional only has quadratic dissipation in terms of $\tilde{v}_{\mathrm{CL}}$ and $\tilde{v}$, in order to ensure the Rayleighian is bounded below, we need enforce the volume constraint $\int_{D(t)} u \,\mathrm{d}x\,\mathrm{d}y = V$. Otherwise, a relaxation model by introducing a dissipation in terms of λ shall be used.

2.3. Onsager's principle and PVIs for an obstacle problem. With the specific driven energy $\mathcal{F}$ on manifold $\mathcal{M}$ and its first variation, we now start to derive the droplets dynamics using Onsager's principle with the obstacle as described below.

2.3.1. Friction damping for the motion of the droplet and the Rayleigh dissipation function. From (2.20), the droplet experiences unbalanced forces $(-F_Y, -F)$ exerted by the environment. These two forces can be modeled as friction forces done by the environment due to the motion of the droplet. First, the contact line friction force density is given by $-F_Y = -\xi v_{\mathrm{CL}}$, where ξ is the friction damping coefficient per unit length for the contact line with the units of mass/(length $\cdot$ time). Second, the friction force density on the capillary surface is given by $-F = -\zeta v_n$, where ζ is the friction damping coefficient per unit area for the capillary surface with the units of mass/(area $\cdot$ time). These are the simplest linear response relations between the unbalanced forces (F_Y, F) and the velocities (v_{CL}, v_n). If one also considers the viscosity dissipation due to the fluids surrounding the capillary surface, we refer to [20] for a nonlocal linear response relation.

Then we introduce the Rayleigh dissipation functional (in the unit of work per unit time) given by [22]

$$Q = \frac{\xi}{2}\int_{\Gamma} |v_{\mathrm{CL}}|^2 \,\mathrm{d}s + \frac{\zeta}{2}\int_{S} |v_n|^2 \,\mathrm{d}s. \tag{2.21}$$

With the geometric configurations, contact line Γ and capillary surface S, the variation of free energy (2.4), and Rayleigh's dissipation functional (2.21), in the next section, we give detailed derivations of the governing equations using Onsager's principle with an obstacle.

2.3.2. Euler–Lagrange equations derived by Onsager's principle. Recast the Rayleigh dissipation functional as a functional of (v_{CL}, v)

$$Q((v_{\mathrm{CL}}, v); \eta) = \frac{\xi}{2}\int_{\Gamma} |v_{\mathrm{CL}}|^2 \,\mathrm{d}s + \frac{\zeta}{2}\int_{D} |v|^2 \frac{1}{\sqrt{1+|\nabla u|^2}} \,\mathrm{d}x\,\mathrm{d}y. \tag{2.22}$$

Define the Rayleighian as

$$\mathrm{Ray}((v_{\mathrm{CL}}, v); \eta) := Q((v_{\mathrm{CL}}, v); \eta) + \dot{\mathcal{F}}((v_{\mathrm{CL}}, v); \eta). \tag{2.23}$$

Then minimizing Rayleighian w.r.t. $(v_{\mathrm{CL}}, v) \in T_\eta M$

$$(v_{\mathrm{CL}}, \partial_t u) = \mathrm{argmin}_{(v_{\mathrm{CL}}, v) \in T_\eta M} \mathrm{Ray}((v_{\mathrm{CL}}, v); \eta) \tag{2.24}$$

yields the Euler–Lagrange equations. Indeed, notice the minimization $(v_{\mathrm{CL}}, \partial_t u)$ satisfies

$$\mathrm{Ray}((v_{\mathrm{CL}} + \varepsilon(\tilde{v}_{\mathrm{CL}} - v_{\mathrm{CL}}), \partial_t u + \varepsilon(\tilde{v} - \partial_t u))) \geq \mathrm{Ray}(v_{\mathrm{CL}}, \partial_t u) \quad \text{for any } ((\tilde{v}_{\mathrm{CL}}, \tilde{v})) \in T_\eta \mathcal{M}. \tag{2.25}$$

Thus taking $\varepsilon \to 0^+$ concludes the following PVI:

$$\begin{aligned} &\text{find } \eta(t) = (\Gamma(t), u(t)) \in \mathcal{M}, \quad (v_{\mathrm{CL}}, \partial_t u) \in T_\eta \mathcal{M} \text{ such that} \\ &\xi v_{\mathrm{CL}} = F_Y \quad \text{on } \Gamma(t), \\ &\zeta \int_{D(t)} \frac{\partial_t u}{\sqrt{1 + |\nabla u|^2}} (\tilde{v} - \partial_t u) \,\mathrm{d}x \,\mathrm{d}y \geq \int_{D(t)} F(\tilde{v} - \partial_t u) \,\mathrm{d}x \,\mathrm{d}y \quad \forall \tilde{v} \in Y_\eta, \\ &\int_{D(t)} u \,\mathrm{d}x \,\mathrm{d}y = V, \end{aligned} \tag{2.26}$$

where $Y_\eta := \{v \in L^2(D); v \geq 0 \text{ on } B_\eta\}$.

By taking $\tilde{v} = 0$ or $\tilde{v} = 2\partial_t u$ in the third equation in (2.26), we have

$$\zeta \int_{D(t)} \frac{|\partial_t u|^2}{\sqrt{1 + |\nabla u|^2}} \,\mathrm{d}x \,\mathrm{d}y = \int_{D(t)} \partial_t u F \,\mathrm{d}x \,\mathrm{d}y. \tag{2.27}$$

Thus plugging the velocity $\tilde{v}_{\mathrm{CL}} = v_{\mathrm{CL}}$ and $\tilde{v} = \partial_t u$ into (2.20), using (2.27) and the second equation in (2.26), we conclude the energy dissipation relation

$$\frac{\mathrm{d}}{\mathrm{d}t} \mathcal{F}(\eta) = -2Q((v_{\mathrm{CL}}, \partial_t u); \eta). \tag{2.28}$$

2.3.3. Equivalent PVIs derived by Onsager's principle w.r.t. virtual displacement. Define a convex subset $K_D := \{v \in C_c^1(D), v \geq 0\}$. We first minimize the Rayleighian defined in (2.23) with any $\tilde{v}_{\mathrm{CL}} \in C(\Gamma)$, and the associated $\tilde{v}$. This gives the same equality $\xi v_{\mathrm{CL}} = F_Y$ for the moving contact line.

Next, we minimize the Rayleighian defined in (2.23) in a subset $(0, \tilde{v}) \subset T_\eta \mathcal{M}$ for any $\tilde{v} \in K_D$. This, together with the equality for the moving contact line, gives a new PVI

$$\begin{aligned} &\text{find } \eta(t) = (\Gamma(t), u(t)) \in \mathcal{M}, \quad (v_{\mathrm{CL}}, \partial_t u) \in T_\eta \mathcal{M} \text{ such that} \\ &\xi v_{\mathrm{CL}} = F_Y \quad \text{on } \Gamma(t), \\ &\zeta \int_{D(t)} \frac{\partial_t u}{\sqrt{1 + |\nabla u|^2}} (\tilde{v} - u) \,\mathrm{d}x \,\mathrm{d}y \geq \int_{D(t)} F(\tilde{v} - u) \,\mathrm{d}x \,\mathrm{d}y, \quad \forall \tilde{v} \in K_D, \\ &\int_{D(t)} u \,\mathrm{d}x \,\mathrm{d}y = V. \end{aligned} \tag{2.29}$$

Indeed, the derivation relies on the fact that for any virtual displacement $\tilde{v} \in K_D$, $u + \varepsilon(\tilde{v} - u) = (1 - \varepsilon)u + \varepsilon\tilde{v}$ is a curve on $\mathcal{M}$ with parameter $0 < \varepsilon < 1$. Thus we

know $(0, \tilde{v}-u) \in T_\eta\mathcal{M}$ and $(0, \partial_t u + \varepsilon(\tilde{v}-u)) \in T_\eta\mathcal{M}$ since $T_\eta\mathcal{M}$ is a convex cone. So (2.29) is concluded after taking minimization for any $(0, \partial_t u + \varepsilon(\tilde{v}-u)) \in T_\eta\mathcal{M}$

$$\mathrm{Ray}((v_{\mathrm{CL}}, \partial_t u + \varepsilon(\tilde{v}-u))) \geq \mathrm{Ray}(v_{\mathrm{CL}}, \partial_t u) \tag{2.30}$$

and letting $\varepsilon \to 0^+$.

By taking $\tilde{v}(\cdot) = u(\cdot,t) \pm \frac{s-t}{2}\partial_t u(\cdot,t)$ and $s \to t^+$ in the third equation of (2.29), we obtain (2.27) and thus we conclude the same energy dissipation relation (2.28).

2.3.4. Strong form of PVI. Using the coincidence set B_η, by taking different $\tilde{v}$, the second equation in (2.26) or in (2.29) can be recast as the same strong form. We have the following proposition on the equivalence of (2.26) and (2.29).

PROPOSITION 2.1. (i) *Let* $(\Gamma(t), u(t))$ *be a smooth solution to the PVI* (2.26). *Then* $(\Gamma(t), u(t)) \in \mathcal{M}$ *satisfies the Euler–Lagrange equation in the strong form*

$$\begin{aligned}
&(v_{CL}, \partial_t u) \in T_\eta\mathcal{M} \ \ \textit{such that}\\
&\xi v_{CL} = F_Y \quad \textit{on } \Gamma(t),\\
&\begin{cases} \zeta \frac{\partial_t u}{\sqrt{1+|\nabla u|^2}} = F & \textit{for } (x,y) \notin B_\eta \textit{ or } F \geq 0\\ \partial_t u = 0 & \textit{for } (x,y) \in B_\eta \textit{ and } F < 0 \end{cases} \qquad \textit{in } D(t),\\
&\int_{D(t)} u \,\mathrm{d}x\,\mathrm{d}y = V.
\end{aligned} \tag{2.31}$$

(ii) *Let* $(\Gamma(t), u(t))$ *be a smooth solution to the PVI* (2.29). *Then* $(\Gamma(t), u(t)) \in \mathcal{M}$ *satisfies the same Euler–Lagrange equation* (2.31).

The proof of this proposition is standard and can be derived by considering different cases that appear in (2.31). From this proposition, we know two PVIs are equivalent and our projection method will rely on PVI (2.29).

Briefly, we will alternately conduct the following two steps. In step (i), we solve the equality governing equations

$$\begin{aligned}
\xi v_{\mathrm{CL}} &= \gamma_{\mathrm{LG}}(\cos\theta_{\mathrm{CL}} - \cos\theta_Y) \quad &\text{on } \Gamma(t),\\
\zeta \frac{\partial_t u}{\sqrt{1+|\nabla u|^2}} &= -\rho g u - \gamma_{\mathrm{LG}} H + \lambda \quad &\text{in } D(t),\\
u &= 0 \quad &\text{on } \Gamma(t),\\
\int_{D(t)} u \,\mathrm{d}x\,\mathrm{d}y &= V
\end{aligned} \tag{2.32}$$

with initial data $\eta(0) = \{\Gamma(0), u(x,y,0)\}$ and initial volume V. Then we do step (ii), the projection to the manifold $\mathcal{M}$. We will discuss the schemes, unconditional stability, and convergence analysis in detail in section 3.

3. Numerical schemes, stability, and convergence analysis. In this section, we first propose a numerical scheme for droplets dynamics with merging and splitting, which are extensions of the first and second order schemes developed in [19] for a single droplet without topological changes. To incorporate the splitting due to an impermeable obstacle, we need to solve the PVI (2.29) instead of PDEs. Inspired by a nonlinear version of the Trotter–Kato product formula, a projection method, which efficiently splits the PDE solver and the obstacle constraint, will be adapted.

Then in section 3.2, we prove the unconditional stability of the projection method for the moving contact line coupled with the motion by mean curvature with an obstacle. In the stability analysis in Proposition 3.1, we focus on the key difficulties due to the moving domain and the obstacle, and consider a droplet placed on a horizontal plane without gravity and volume constraint. Finally, in section 3.3 we include the gravity and the volume constraint and give a convergence analysis of the projection method for droplets with a pinning contact line; see Theorem 3.3.

3.1. Numerical schemes based on explicit boundary moving and the projection method. In this subsection, we present a numerical scheme for PVI (2.29) describing the droplet dynamics with merging and splitting. First, we further split the equality solver for (2.32) into two steps: (i) explicit boundary updates and (ii) semi-implicit capillary surface updates. The unconditional stability for the explicit 1D boundary updates is proved in [19], which efficiently decouples the computations of the boundary evolution and the capillary surface updates. The semi-implicit capillary surface updates without obstacles but with the volume constraint can be converted to a standard elliptic solver at each step. Next, to enforce the impermeable obstacle, (iii) we project the capillary surface to the manifold $\mathcal{M}$. This step has an explicit formula so also keeps the efficiency. Finally, to incorporate the phase transition information at splitting points, (iv) we detect splitting points after a threshold and add new contact line updates after that; see detailed explanations for the phase transition at emerged contact lines in section 3.1.1. The current presentation for the proposed projection method focuses only on 1D wetting domain. There are many well-developed numerical methods for free boundary problems in high dimensions that can be adapted such as the grid-based particle method [30], the immersed boundary method [31], the level-set method [45], and the threshold dynamics method [42].

3.1.1. PVI for 2D droplet placed on a groove-textured and inclined surface. For simplicity in presentation, we only describe numerical schemes for 2D droplets. Hence we first use the PVI obtained in (2.29) to derive the governing PVI for a 2D droplet placed on a groove-textured and inclined surface and explain the phase transition happening at emerged contact lines after splitting.

Given a groove-textured impermeable surface described by a graph function $w(x)$, a droplet is then described by $A := \{(x, y); a \le x \le b, w(x) \le y \le u(x) + w(x)\}$. Following the convention, we use the Cartesian coordinate system built on an inclined plane with effective inclined angle θ_0 such that $-\frac{\pi}{2} < \theta_0 < \frac{\pi}{2}$ and $(\tan\theta_0)x$ is the new x-axis; see Figure 1. Denote the height function as

$$h(x,t) := u(x,t) + w(x).$$

To be consistent with height function u in the last section, we choose the configuration states of this droplet as the relative height function (capillary surface) $u(x,t) \ge 0$ and partially wetting domain $a(t) \le x \le b(t)$ with free boundaries $a(t), b(t)$. Consider the manifold

$$\mathcal{M} := \{a, b, u(x);\ u(x) \ge 0,\ u(x) \in C_0^2(a,b) \cap L^2(a,b)\}. \tag{3.1}$$

Consider the energy functional associated with the groove-textured surface

$$\begin{aligned}\mathcal{F}(\eta) = {} & \gamma_{\mathrm{LG}} \int_a^b \sqrt{1 + (\partial_x(u+w))^2}\,\mathrm{d}x + (\gamma_{\mathrm{SL}} - \gamma_{\mathrm{SG}}) \int_a^b \sqrt{1 + (\partial_x w)^2}\,\mathrm{d}x \\ & + \rho g \int_a^b \int_{h_0}^{u+h_0} (y\cos\theta_0 + x\sin\theta_0)\,\mathrm{d}y\,\mathrm{d}x,\end{aligned} \tag{3.2}$$

where ρ is the density of the liquid and g is the gravitational acceleration. Then we have

$$
\begin{aligned}
G(u,x) &= \sqrt{1+(\partial_x(u+w))^2} + \sigma\sqrt{1+(\partial_x w)^2} \\
&\quad + \frac{\rho g}{\gamma_{\mathrm{LG}}}\left(\frac{u^2\cos\theta_0}{2} + \cos\theta_0 uw + x\sin\theta_0 u\right) \\
\partial_u G &= \frac{\rho g}{\gamma_{\mathrm{LG}}}\left((u+w)\cos\theta_0 + x\sin\theta_0\right), \quad \partial_{u_x} G = \frac{\partial_x(u+w)}{\sqrt{1+(\partial_x(u+w))^2}}.
\end{aligned} \tag{3.3}
$$

Remark 1. Let the density of gas outside the droplet be $\rho_0 = 0$. We denote the capillary coefficient as $\varsigma := \frac{\rho g}{\gamma_{\mathrm{LG}}} > 0$ and the capillary length as $L_c := \frac{1}{\sqrt{\varsigma}}$. For a droplet with volume V, its equivalent length (characteristic length) L is defined as $V = \frac{4\pi}{3}L^3$ in three dimensions and $V = \pi L^2$ in two dimensions. The Bond number $\mathrm{Bo} := (\frac{L}{L_c})^2 = \varsigma L^2$ shall be small enough to observe the capillary effect [12]. In the inclined case, for a droplet with volume V in two dimensions, the effective Bond number is $\mathrm{Bo} := (\frac{L}{L_c})^2\cos\theta_0 = \varsigma L^2\cos\theta_0$. After the dimensionless argument, we use new dimensionless quantities β, κ, V in the governing equation below.

Recall $K_D = \{v \in C_c^1(D), v \geq 0\}$. Then by the same derivations as (2.29), we have the governing PVI for the 2D droplet,

$$
\begin{aligned}
&\int_{a(t)}^{b(t)} \left(\beta\frac{\partial_t h(x,t)}{\sqrt{1+(\partial_x h)^2}} - \frac{\partial}{\partial x}\left(\frac{\partial_x h}{\sqrt{1+(\partial_x h)^2}}\right) + \kappa(h\cos\theta_0 + x\sin\theta_0) - \lambda(t)\right)(\tilde{v}-u)\,\mathrm{d}x \geq 0 \\
&\qquad\qquad \text{for any } \tilde{v}(x) \in K_{D(t)}, \\
&\qquad\qquad h = u + w, \quad u \geq 0 \quad \text{in } D(t), \\
&\qquad\qquad u(a(t),t) = u(b(t),t) = 0, \\
&a'(t) = \sigma\sqrt{1+(\partial_x w)^2} + \frac{1+\partial_x h\partial_x w}{\sqrt{1+(\partial_x h)^2}}\Big|_{x=a} = \frac{1}{\cos\theta_{0a}}(\cos\theta_a - \cos\theta_Y), \\
&b'(t) = -\sigma\sqrt{1+(\partial_x w)^2} - \frac{1+\partial_x h\partial_x w}{\sqrt{1+(\partial_x h)^2}}\Big|_{x=b} = -\frac{1}{\cos\theta_{0b}}(\cos\theta_b - \cos\theta_Y), \\
&\qquad\qquad \int_{a(t)}^{b(t)} u(x,t)\,\mathrm{d}x = V,
\end{aligned} \tag{3.4}
$$

where θ_a, θ_b are two contact angles at $a(t)$, $b(t)$ and $\partial_x w|_a = \tan\theta_{0a}$, $\partial_x h|_a = \tan(\theta_{0a}+\theta_a)$ and $\partial_x w|_b = -\tan\theta_{0b}$ and $\partial_x h|_b = -\tan(\theta_{0b}+\theta_b)$; see Figure 1. It is easy to check the steady state $a'(t) = b'(t) = 0$ recovers Young's angle condition.

The PVI above is able to describe the merging and splitting of several drops. However, whenever topological changes happen, (2.29) cannot describe the correct phase transition at the splitting/merging points. For instance, when one droplet splits into two droplets, physically, at the splitting domain $D_0 := \{(x,y) \in D\backslash\Gamma;\, u(x,t) = 0\}$, the interface between gas and liquid becomes the interface between gas and solid, therefore new contact lines with competitions from three phases appear. Instead, the dynamics governing by PVI (2.29) does not contain this phase transition information but only leads to a nonphysical motion at the splitting domain D_0, i.e., a droplet is allowed to move along the boundary D_0. We propose the following natural method to incorporate the phase transition information into dynamics after splitting. (I) We first detect when and where the phase transition happens by recording the new generated contact lines. (II) Then surface energies from three phases take over the

dynamics posterior to splitting. That is to say, the generated two droplets have the same governing equation with (2.29), respectively, and the volume of each droplet is preserved over time; see Step 5 in the algorithm below.

3.1.2. First order numerical scheme: Explicit boundary updating with the projection method.

Step 1. *Explicit boundary updates.* Compute the one-side approximated derivative of h^n at b^n and a^n, denoted as $(\partial_x h^n)_N$ and $(\partial_x h^n)_0$. Then by the dynamic boundary condition in (3.4), we update a^{n+1}, b^{n+1} using

$$\begin{aligned}\frac{a^{n+1}-a^n}{\Delta t} &= \sigma\sqrt{1+(\partial_x w)_0^2}+\frac{1+(\partial_x h^n)_0(\partial_x w)_0}{\sqrt{1+(\partial_x h^n)_0^2}},\\ \frac{b^{n+1}-b^n}{\Delta t} &= -\sigma\sqrt{1+(\partial_x w)_N^2}-\frac{1+(\partial_x h^n)_N(\partial_x w)_N}{\sqrt{1+(\partial_x h^n)_N^2}}.\end{aligned} \tag{3.5}$$

Step 2. Rescale h^n from $[a^n, b^n]$ to $[a^{n+1}, b^{n+1}]$ with $O(\Delta t^2)$ accuracy using an arbitrary Lagrangian–Eulerian discretization. For $x^{n+1} \in [a^{n+1}, b^{n+1}]$, denote the map from moving grids at t^{n+1} to t^n as

$$x^n := a^n + \frac{b^n - a^n}{b^{n+1}-a^{n+1}}(x^{n+1}-a^{n+1}) \in [a^n, b^n]. \tag{3.6}$$

Define the rescaled solution for h^n as

$$h^{n*}(x^{n+1}) := h^n(x^n) + \partial_x h^n(x^n)(x^{n+1}-x^n). \tag{3.7}$$

It is easy to verify by using the Taylor expansion $h^{n*}(x^{n+1}) = h^n(x^{n+1}) + O(|x^n - x^{n+1}|^2)$; see [19, Appendix B]

Step 3. *Capillary surface updates without impermeable obstacle constraint, but with volume preserving constraint.* Update $\tilde{h}^{n+1}$ and λ^{n+1} semi-implicitly.

$$\begin{aligned}&\frac{\beta}{\sqrt{1+(\partial_x h^{n*})^2}}\frac{\tilde{h}^{n+1}-h^{n*}}{\Delta t}\\ &\quad=\frac{\partial}{\partial x}\left(\frac{\partial_x \tilde{h}^{n+1}}{\sqrt{1+(\partial_x h^{n*})^2}}\right)-\kappa(h^{n+1}\cos\theta_0 + x^{n+1}\sin\theta_0)+\lambda^{n+1},\\ &\tilde{h}^{n+1}(a^{n+1}) = w(a^{n+1}),\quad \tilde{h}^{n+1}(b^{n+1}) = w(b^{n+1}),\\ &\int_{a^{n+1}}^{b^{n+1}} \tilde{u}^{n+1}(x^{n+1})\,\mathrm{d}x^{n+1} = V,\end{aligned} \tag{3.8}$$

where the independent variable is $x^{n+1} \in (a^{n+1}, b^{n+1})$.

Step 4. *Enforce the impermeable obstacle condition by the projection.* Find h^{n+1} and λ satisfying

$$\begin{cases} h^{n+1} = \max\{\tilde{h}^{n+1}+\lambda, w\},\\ \int_D h^{n+1}\,\mathrm{d}x\,\mathrm{d}y = V + \int_D w\,\mathrm{d}x\,\mathrm{d}y. \end{cases} \tag{3.9}$$

This is indeed project $\tilde{h}$ to the manifold $\mathcal{M}$ with the volume constraint V of the droplet; see Lemma 3.2. (3.9) can be implemented using a bisection search for λ.

Step 5. *Phase transition and emerged triple points.* Let $\varepsilon > 0$ be a threshold parameter. If the length of splitting domain $D_0 > \varepsilon$, then record two new endpoints c^{n+1}, d^{n+1} (emerged triple points). Regard the current profile h^{n+1} on (a^{n+1}, c^{n+1}) and (d^{n+1}, b^{n+1}) as two independent droplets and enforce the moving contact line boundary conditions at these two emerged triple points c^{n+1}, d^{n+1}. The total volume of these two droplet remains the same.

First order scheme for merging. The numerical scheme for the dynamics of two independent droplets with endpoints a_1^n, b_1^n (a_2^n, b_2^n, resp.) are the same as those in Steps 1–3. To detect the merging of two independent droplets, at each time stepping t^n, one also needs a threshold parameter $\varepsilon > 0$ such that we treat two droplets as one big droplet if $|a_2^n - b_1^n| < \varepsilon$.

The projection method for droplets dynamics above also works for the second order scheme, which replaces Steps 1–3 by a midpoint scheme. We omit details and refer to [19].

Remark 2. In Step 5, the additional moving contact line boundary condition at the emerged triple points after splitting is just a numerical algorithm to realize the phase transitions from two phases to three phases. To model this procedure in a variational formulation is still an open question. In the following stability analysis, convergence analysis, and accuracy check, we will not include Step 5 for the enforced phase transition at emerged triple points.

3.2. Unconditional stability of the projection method for the moving contact line and the motion by mean curvature. In this section, we show the unconditional stability of the projection method for the moving contact line and the motion by mean curvature. To focus on the key difficulties due to the moving domain and the obstacle, we present an unconditional stability analysis for the case the droplet is placed on a flat horizontal plane without the gravity and the volume constraint. We will first present a projection method with a small modification for the mean curvature term in (3.13).

3.2.1. A projection method for the moving contact line and the motion by mean curvature. To focus on the moving contact line and the obstacle problem, we first present a simplified projection method for droplets placed on a horizontal plane without the gravity and the volume constraint.

Step 1. *Explicit boundary updates.* We update a^{n+1}, b^{n+1} using

$$\frac{a^{n+1} - a^n}{\Delta t} = \sigma + \frac{1}{\sqrt{1 + (\partial_x h^n)^2}}\Big|_{a^n}, \quad \frac{b^{n+1} - b^n}{\Delta t} = -\sigma - \frac{1}{\sqrt{1 + (\partial_x h^n)^2}}\Big|_{b^n}. \tag{3.10}$$

Step 2. Rescale h^n from $[a^n, b^n]$ to $[a^{n+1}, b^{n+1}]$ such that

$$h^{n*}(x^{n+1}) := h^n(x^n) = U(Z), \quad x^{n+1} \in [a^{n+1}, b^{n+1}], \tag{3.11}$$

where $Z \in [0, 1]$ is a fixed domain variable satisfying

$$Z = \frac{x^n - a^n}{b^n - a^n} = \frac{x^{n+1} - a^{n+1}}{b^{n+1} - a^{n+1}}. \tag{3.12}$$

Step 3. *Capillary surface updates without impermeable obstacle constraint.* Update $\tilde{h}^{n+1}$ implicitly,

$$\frac{\beta}{\sqrt{1+(\partial_x\tilde{h}^{n+1})^2}}\frac{\tilde{h}^{n+1}-h^{n*}}{\Delta t}=\frac{\partial}{\partial x}\left(\frac{\partial_x\tilde{h}^{n+1}+\partial_x h^{n*}}{\sqrt{1+(\partial_x\tilde{h}^{n+1})^2}+\sqrt{1+(\partial_x h^{n*})^2}}\right), \tag{3.13}$$
$$\tilde{h}^{n+1}(a^{n+1})=0,\quad \tilde{h}^{n+1}(b^{n+1})=0,$$

where the independent variable is $x^{n+1}\in(a^{n+1},b^{n+1})$.

Step 4. *Projection due to the impermeable obstacle.*

$$h^{n+1}=\max\{\tilde{h}^{n+1},0\}. \tag{3.14}$$

3.2.2. Unconditional stability for the projection method. Now we prove a proposition for the unconditional stability of the simplified projection method above.

PROPOSITION 3.1. *For any $T>0$, let Δt be the time step and $N=\frac{T}{\Delta t}$. Suppose h^n, h^{n^*}, and $\tilde{h^n}$ are obtained from the above projection method. Then we have the following stability estimates:*

(i) *for endpoints,*

$$a^0+\sigma T\le a^n\le a^0+(1+\sigma)T,\qquad b^0-(1+\sigma)T\le b^n\le b^0-\sigma T; \tag{3.15}$$

(ii) *for the capillary surface,*

$$\max_{1\le n\le N}\int_{a^n}^{b^n}\sqrt{1+|\partial_x h^n|^2}\,\mathrm{d}x+\frac{\beta}{\Delta t}\sum_{n=0}^{N-1}\int_{a^{n+1}}^{b^{n+1}}\frac{|\tilde{h}^{n+1}-h^{n*}|^2}{\sqrt{1+(\partial_x\tilde{h}^{n+1})^2}}\,\mathrm{d}x \tag{3.16}$$
$$\le 8T+2\int_{a^0}^{b^0}\sqrt{1+(\partial_x h^0)^2}\,\mathrm{d}x.$$

Proof. First, we give the stability estimates for endpoints a^n,b^n.

From (3.10), we know

$$\sigma\Delta t\le a^{n+1}-a^n\le(\sigma+1)\Delta t,\quad -(\sigma+1)\Delta t\le b^{n+1}-b^n\le-\sigma\Delta t. \tag{3.17}$$

Then telescoping shows (3.15).

Second, we give the stability estimates for $\tilde{h}^n$.

From (3.18) and elementary calculations we list the following expressions in terms of the Z variable:

(3.18)
$$h^n(x^n)=U(Z)=h^{n*}(x^{n+1}),\quad \partial_x h^n(x^n)=\frac{\partial_Z U(Z)}{b^n-a^n},\quad \partial_x h^{n*}(x^{n+1})=\frac{\partial_Z U(Z)}{b^{n+1}-a^{n+1}}.$$

Multiplying (3.13) by $v:=\tilde{h}^{n+1}-h^{n*}$ and integrating from a^{n+1} to b^{n+1}, we obtain

(3.19)
$$\frac{\beta}{\Delta t}\int_{a^{n+1}}^{b^{n+1}}\frac{|\tilde{h}^{n+1}-h^{n*}|^2}{\sqrt{1+(\partial_x\tilde{h}^{n+1})^2}}\,\mathrm{d}x+\int_{a^{n+1}}^{b^{n+1}}\frac{|\partial_x\tilde{h}^{n+1}|^2-|\partial_x h^{n*}|^2}{\sqrt{1+(\partial_x\tilde{h}^{n+1})^2}+\sqrt{1+(\partial_x h^{n*})^2}}\,\mathrm{d}x=0.$$

This gives

(3.20)
$$\frac{\beta}{\Delta t}\int_{a^{n+1}}^{b^{n+1}}\frac{|\tilde{h}^{n+1}-h^{n*}|^2}{\sqrt{1+(\partial_x\tilde{h}^{n+1})^2}}\,\mathrm{d}x+\int_{a^{n+1}}^{b^{n+1}}\left(\sqrt{1+(\partial_x\tilde{h}^{n+1})^2}-\sqrt{1+(\partial_x h^{n*})^2}\right)\mathrm{d}x=0.$$

We now prove the following claim:

$$\int_{a^{n+1}}^{b^{n+1}} \sqrt{1+(\partial_x h^{n*})^2}\,\mathrm{d}x - \int_{a^n}^{b^n} \sqrt{1+(\partial_x h^n)^2}\,\mathrm{d}x \le 4\Delta t. \tag{3.21}$$

Proof of the claim (3.21). First, from (3.17) and $|\sigma| < 1$, we know

$$\left|(b^{n+1}-a^{n+1}) - (b^n - a^n)\right| \le 4\Delta t. \tag{3.22}$$

Second, by changing variables (3.18), we have

$$\begin{aligned}
&\int_{a^{n+1}}^{b^{n+1}} \sqrt{1+(\partial_x h^{n*})^2}\,\mathrm{d}x - \int_{a^n}^{b^n} \sqrt{1+(\partial_x h^n)^2}\,\mathrm{d}x \\
&= \int_0^1 \sqrt{(b^{n+1}-a^{n+1})^2 + \left(\partial_Z U(Z)\right)^2}\,\mathrm{d}Z - \int_0^1 \sqrt{(b^n-a^n)^2+(\partial_Z U(Z))^2}\,\mathrm{d}Z \\
&= \int_0^1 \frac{(b^{n+1}-a^{n+1})^2 - (b^n-a^n)^2}{\sqrt{(b^{n+1}-a^{n+1})^2 + \left(\partial_Z U(Z)\right)^2} + \sqrt{(b^n-a^n)^2+(\partial_Z U(Z))^2}}\,\mathrm{d}Z.
\end{aligned} \tag{3.23}$$

Therefore, from (3.22), we know

$$\begin{aligned}
&\left|\int_{a^{n+1}}^{b^{n+1}} \sqrt{1+(\partial_x h^{n*})^2}\,\mathrm{d}x - \int_{a^n}^{b^n} \sqrt{1+(\partial_x h^n)^2}\,\mathrm{d}x\right| \\
&\qquad \le \frac{\left|(b^{n+1}-a^{n+1})^2 - (b^n-a^n)^2\right|}{\sqrt{(b^{n+1}-a^{n+1})^2} + \sqrt{(b^n-a^n)^2}} \le 4\Delta t.
\end{aligned} \tag{3.24}$$

∎

From this claim, (3.20) becomes

$$\begin{aligned}
&\frac{\beta}{\Delta t}\int_{a^{n+1}}^{b^{n+1}} \frac{|\tilde{h}^{n+1}-h^{n*}|^2}{\sqrt{1+(\partial_x \tilde{h}^{n+1})^2}}\,\mathrm{d}x + \int_{a^{n+1}}^{b^{n+1}} \sqrt{1+(\partial_x \tilde{h}^{n+1})^2}\,\mathrm{d}x \\
&\quad - \int_{a^n}^{b^n} \sqrt{1+(\partial_x h^n)^2}\,\mathrm{d}x \le 4\Delta t.
\end{aligned} \tag{3.25}$$

Third, we give the estimate for h^n.

We prove by induction. For $n = 0$, from (3.25) and the Dirichlet boundary condition we know $\tilde{h}^1 \in W^{1,1}(a^1, b^1)$. Thus

$$\partial_x h^1 = \partial_x(\tilde{h}^1_+) = \mathrm{sgn}(\tilde{h}^1)\partial_x \tilde{h}^1 \in L^1(a^1, b^1). \tag{3.26}$$

This implies

$$\int_{a^1}^{b^1} \sqrt{1+|\partial_x h^1|^2}\,\mathrm{d}x \le \int_{a^1}^{b^1} \sqrt{1+|\partial_x \tilde{h}^1|^2}\,\mathrm{d}x. \tag{3.27}$$

Then by induction, (3.25) becomes

$$\begin{aligned}
&\frac{\beta}{\Delta t}\int_{a^{n+1}}^{b^{n+1}} \frac{|\tilde{h}^{n+1}-h^{n*}|^2}{\sqrt{1+(\partial_x \tilde{h}^{n+1})^2}}\,\mathrm{d}x + \int_{a^{n+1}}^{b^{n+1}} \sqrt{1+(\partial_x h^{n+1})^2}\,\mathrm{d}x \\
&\quad - \int_{a^n}^{b^n} \sqrt{1+(\partial_x h^n)^2}\,\mathrm{d}x \le 4\Delta t.
\end{aligned} \tag{3.28}$$

By telescoping, we obtain

$$\int_{a^{n+1}}^{b^{n+1}} \sqrt{1+(\partial_x h^{n+1})^2}\,\mathrm{d}x \le 4T + \int_{a^0}^{b^0} \sqrt{1+(\partial_x h^0)^2}\,\mathrm{d}x \tag{3.29}$$

and thus we conclude (3.16). ∎

Remark 3. We remark that this proposition only holds for the 1D wetting domain case because the estimates in Proposition 3.1 rely on the estimates for the normal velocity of the contact points $a(t), b(t)$. Indeed, the 2D contact line motion is definitely a challenging problem in the geometric measure theory, even for a pure motion by mean curvature without obstacles. With the volume preserving constraint, we refer to [35] for a construction of global distributional solutions for mean curvature flow in high dimensions, which used a discrete-time gradient flow approach following the classical results developed in [2, 32]. For stability analysis for the contact line problem in high dimensions, using a similar discrete-time gradient flow approach, [17] also constructed a unique global solution starting from a star-shaped initial wetting domain but with additional assumptions: (i) under a quasi-static assumption for the capillary surface; (ii) replacing the surface energy by the Dirichlet energy. Their stability result states that the wetting domain maintains its star-shape dynamically.

3.3. Convergence analysis of the projection method with pinning contact lines. In this section, we give a convergence analysis for the projection method under the pinning contact line assumption. On the one hand, the pinning (or sticking) effect is an important observed phenomenon in most droplet wetting applications [13, 38, 12]. On the other hand, the convergence analysis of the projection method for the original moving contact line problem is very challenging. In the following subsections, we first represent the PVI solution with pinning contact line as a nonlinear semigroup solution, then introduce the associated projection method and its resolvent representation, and finally give the convergence analysis of the projection method using a nonlinear version of the Trotter–Kato product formula.

3.3.1. Pinning contact line and the associated PVI. In order to work in a Hilbert space $X := L^2(D)$, we clarify the following two assumptions on the Rayleigh dissipation functional Q. Recall (2.22). First, we replace the dissipation due to the motion of the capillary surface as $\zeta \int_D |v|^2\,\mathrm{d}x\,\mathrm{d}y$ so

$$\tilde{Q} := \frac{\xi}{2}\int_\Gamma |v_{\mathrm{CL}}|^2\,\mathrm{d}s + \frac{\zeta}{2}\int_D |v|^2\,\mathrm{d}x\,\mathrm{d}y. \tag{3.30}$$

Second, we assume the friction coefficient $\xi \to +\infty$, which leads to the pinning boundary condition $v_{\mathrm{CL}} = 0$. Then the PVI (2.29) becomes the following parabolic obstacle problem in a fixed domain D. Denote $K_D := \{u \in L^2(D); u \ge 0\}$.

$$\begin{aligned} &\text{Find } u(t) \in K_D \cap C_0(D),\ \lambda(t) \in \mathbb{R} \ \text{ such that} \\ &\zeta \int_D \partial_t u(\tilde{v}-u)\,\mathrm{d}x\,\mathrm{d}y \ge \int_D F(\tilde{v}-u)\,\mathrm{d}x\,\mathrm{d}y \quad \forall \tilde{v} \in K_D \cap C_0(D), \\ &\int_D u\,\mathrm{d}x\,\mathrm{d}y = V, \end{aligned} \tag{3.31}$$

where $F = \gamma_{\mathrm{LG}}\nabla\cdot(\frac{\nabla u}{\sqrt{1+|\nabla u|^2}}) - \rho g u + \lambda$.

3.3.2. The sum of two maximal monotone operators and the nonlinear semigroup solution. To prove the convergence using the Trotter–Kato product formula for two maximal monotone operators, we shall first convert the original gradient flow problem with volume constraint to a problem in a linear subspace. To do this, choose any fixed capillary profile $u^* \in C_0^2(D)$ satisfying $\int_D u^* \,\mathrm{d}x\,\mathrm{d}y = V$, $u^* \geq 0$ as a reference. We introduce a Hilbert space

$$X_1 := \left\{ v \in L^2(D); \int_D v \,\mathrm{d}x\,\mathrm{d}y = 0 \right\}. \tag{3.32}$$

Define a functional E from X_1 to $[0, +\infty]$

$$E(v) := \mathcal{F}(v + u^*) = \gamma_{\mathrm{LG}} \int_D \sqrt{1 + |\nabla(v + u^*)|^2} \,\mathrm{d}x\,\mathrm{d}y + \rho g \int_D \frac{(v + u^*)^2}{2} \,\mathrm{d}x\,\mathrm{d}y. \tag{3.33}$$

First, it is easy to verify that E is a proper, convex, and lower semicontinuous functional on X_1. Second, in X_1, we compute the Gâteaux derivative of E: for any $\tilde{v} \in X_1$,

$$\frac{\mathrm{d}}{\mathrm{d}\varepsilon}\Big|_{\varepsilon=0} E(v + \varepsilon\tilde{v}) = \left\langle -\gamma_{\mathrm{LG}} \nabla \cdot \left(\frac{\nabla(v + u^*)}{\sqrt{1 + |\nabla(v + u^*)|^2}} \right) + \rho g (v + u^*) - \lambda, \tilde{v} \right\rangle \tag{3.34}$$

for any constant $\lambda \in \mathbb{R}$. Indeed, any constants are zero element in $(X_1)'$. Thus we know the subdifferential of E in X_1 is single-valued and agrees with the Gâteaux derivative, denoted as

$$\nabla E(v) := -\gamma_{\mathrm{LG}} \nabla \cdot \left(\frac{\nabla(v + u^*)}{\sqrt{1 + |\nabla(v + u^*)|^2}} \right) + \rho g (v + u^*) - \lambda. \tag{3.35}$$

Since E is a proper, convex, and lower semicontinuous functional on X_1, we know ∇E is a maximal monotone operator which generates a nonlinear C_0-semigroup, symbolically denoted as $S_1(t) := e^{-t\nabla E}$; cf. [5, 25]. The semigroup solution $u(t) = v(t) + u^*$ satisfies the following governing equations:

$$\begin{aligned} \zeta \partial_t u = \gamma_{\mathrm{LG}} \nabla \cdot \left(\frac{\nabla u}{\sqrt{1 + |\nabla u|^2}} \right) - \rho g u + \lambda \quad &\text{in } D, \\ u = 0 \quad &\text{on } \partial D, \\ \int_D u \,\mathrm{d}x\,\mathrm{d}y = V. & \end{aligned} \tag{3.36}$$

Notice the left-hand side in the first equation above is the vertical velocity instead of the normal velocity of the capillary surface due to the special choice of $\tilde{Q}$ in (3.30).

For the obstacle problem (3.31), we need to introduce an indicator functional I_K for the convex subset

$$K := \{ v \in X_1; u^* + v \geq 0 \} \subset X_1, \tag{3.37}$$

where $u^* + K$ is indeed a convex cone. Denote $A := \nabla E$, $B := \partial I_K$. Since $A + B = \nabla E + \partial I_K$ is a maximal monotone operator in X_1, $A + B$ generates a strongly continuous semigroup on $[0, +\infty)$ of contractions [29, 5], symbolically denoted as $S(t) := e^{-t(\nabla E + \partial I_K)}$. For any $u_0 = v_0 + u^*$, $v_0 \in K$, the unique mild solution to (3.31) is given by [5]

$$u(t) = e^{-t(\nabla E + \partial I_K)} u_0 := u^* + e^{-t(\nabla E + \partial I_K)} v_0. \tag{3.38}$$

3.3.3. Projection method and resolvent representation. To numerically solve the obstacle problem (3.31) generated by $A + B$, the projection method (the splitting method) is a natural and efficient method. Its convergence will be shown below by using a nonlinear version of the Trotter–Kato product formula [25].

We first present the projection method for (3.31) in terms of the abstract operators ∇E and ∂I_K as follows. As mentioned in the introduction (see (1.3)), we will see this is exactly a splitting approximation of the minimizing movement method. For $\tau := \frac{T}{n}$, we use the projection method to construct an approximation u^k of $u(t^k)$ with $t^k = k\tau$, $k = 0, 1, \ldots, n$, below.

Step (i) For $u^k = v^k + u^*$, $v^k \in K$, find

$$\tilde{u}^{k+1} = u^* + \operatorname{argmin}_{v \in X_1} \left(E(v) + \frac{\|v - v^k\|^2}{2\tau} \right), \tag{3.39}$$

which is symbolically given by

$$\tilde{u}^{k+1} = (I + \tau \nabla E)^{-1} u^k. \tag{3.40}$$

Step (ii) Find u^{k+1} and λ satisfying

$$\begin{cases} u^{k+1} = \max\{\tilde{u}^{k+1} + \lambda,\, 0\}, \\ \int_D u^{k+1}\, \mathrm{d}x\, \mathrm{d}y = V. \end{cases} \tag{3.41}$$

Indeed, we have the following lemma characterizing the projection operator in Step (ii).

LEMMA 3.2. *Let $u^* \geq 0$ be a reference profile satisfying $\int_D u^*\, \mathrm{d}x = V$. Given $\tilde{u}^{k+1}$, denote $\tilde{v}^{k+1} = \tilde{u}^{k+1} - u^*$. The following problems are equivalent:*

(i) *Find $u^{k+1} = v^{k+1} + u^*$ with v^{k+1} satisfying*

$$\begin{cases} v^{k+1} \in K, \\ \langle \tilde{v}^{k+1} - v^{k+1}, \phi - v^{k+1} \rangle \leq 0 \quad \forall \phi \in K. \end{cases} \tag{3.42}$$

(ii) *Find $u^{k+1} = v^{k+1} + u^*$ with v^{k+1} satisfying*

$$\tilde{v}^{k+1} - v^{k+1} \in \tau \partial I_K(v^{k+1}) \quad \forall \tau > 0. \tag{3.43}$$

(iii) *Find $u^{k+1} = v^{k+1} + u^*$ with v^{k+1} satisfying $v^{k+1} = \mathrm{Proj}_K(\tilde{u}^{k+1} - u^*)$.*

(iv) *Find u^{k+1} and λ satisfying* (3.41).

Proof. First, we prove (i) is equivalent to (ii).

The subdifferential of I_K at $v \in K$ in X_1 is given by

$$f \in \tau \partial I_K(v) \Longleftrightarrow 0 \geq \langle f, \phi - v \rangle \quad \forall \phi \in K. \tag{3.44}$$

Thus ∂I_K is a convex cone and

$$\begin{aligned} &\tilde{u}^{k+1} - u^{k+1} = \tilde{v}^{k+1} - v^{k+1} \in \tau \partial I_K(v^{k+1}) \\ \Longleftrightarrow &\begin{cases} v^{k+1} \in K, \\ \langle \tilde{v}^{k+1} - v^{k+1}, \phi - v^{k+1} \rangle \leq 0 \quad \forall \phi \in K. \end{cases} \end{aligned} \tag{3.45}$$

Second, the equivalence between (i) and (iii) can be directly verified since

$$\begin{cases} v^{k+1} \in K, \\ \langle \tilde{v}^{k+1} - v^{k+1}, \phi - v^{k+1} \rangle \leq 0 \quad \forall \phi \in K \end{cases} \Longleftrightarrow v^{k+1} = \mathrm{Proj}_K(\tilde{v}^{k+1}). \tag{3.46}$$

Third, we prove the equivalence between (iii) and (iv). First (iii) is equivalent to finding the projection of $\tilde{u}^{k+1}$ in the set $u^* + K$, i.e.,

$$u^{k+1} = u^* + \mathrm{Proj}_K(\tilde{u}^{k+1} - u^*) = \mathrm{Proj}_{u^*+K}(\tilde{u}^{k+1}). \tag{3.47}$$

Notice the following two sets are the same:

$$u^* + K = K_D \cap \left\{ u; \int u \,\mathrm{d}x\,\mathrm{d}y = V \right\}, \tag{3.48}$$

where $K_D = \{u \in L^2(D); u \geq 0\}$. Then (iii) is equivalent to finding the projection of $u^{\tilde{k+1}}$ in $K_D \cap \{u; \int u \,\mathrm{d}x\,\mathrm{d}y = V\}$, i.e.,

$$(u^{k+1}, \lambda^*) = \arg \min_{u \in K_D, \lambda \in \mathbb{R}} L(u, \lambda), \tag{3.49}$$

where λ is a Lagrange multiplier and

$$L(u, \lambda) := \frac{1}{2}\|u - \tilde{u}^{k+1}\|^2 - \lambda \left(\int_D u \,\mathrm{d}x\,\mathrm{d}y - V \right).$$

If $(u^{k+1}, \lambda^*) = \arg\min_{u \in K_D, \lambda \in \mathbb{R}} L(u, \lambda)$, then (u^{k+1}, λ^*) satisfies

$$L(u^{k+1}, \lambda^*) \leq L(u^{k+1} + \varepsilon(\tilde{\phi} - u^{k+1}), \lambda^* + \varepsilon\mu) \quad \forall 0 < \varepsilon < 1, \tilde{\phi} \in K_D, \mu \in \mathbb{R}. \tag{3.50}$$

This is equivalent to

$$0 \leq \langle (\tilde{\phi} - u^{k+1}), (u^{k+1} - \tilde{u}^{k+1}) \rangle - \mu \left(\int_D u^{k+1} \,\mathrm{d}x\,\mathrm{d}y - V \right) - \lambda^* \int_D (\tilde{\phi} - u^{k+1}) \,\mathrm{d}x\,\mathrm{d}y + O(\varepsilon) \tag{3.51}$$

for any $0 < \varepsilon < 1$, any $\tilde{\phi} \in \tilde{K}$, and any $\mu \in \mathbb{R}$.

Taking $\varepsilon \to 0^+$, from the arbitrariness of $\tilde{\phi} \in \tilde{K}$, $\mu \in \mathbb{R}$, we have $\int_D u^{k+1} \,\mathrm{d}x\,\mathrm{d}y = V$. Thus (3.51) is equivalent to

$$\begin{cases} \int_D u^{k+1} \,\mathrm{d}x\,\mathrm{d}y = V, \\ \langle u^{k+1} - \tilde{u}^{k+1}, \tilde{\phi} - u^{k+1} \rangle - \lambda^* \int_D (\tilde{\phi} - u^{k+1}) \,\mathrm{d}x\,\mathrm{d}y \geq 0, \quad \tilde{\phi} \in \tilde{K}. \end{cases} \tag{3.52}$$

Therefore, the equivalence of (3.52) with (3.41) can be directly concluded from [27, p. 27], provided there exists solution (u^{k+1}, λ^*) to (3.41). Define

$$f(\lambda) := \int_D \max\{\tilde{u}^{k+1} + \lambda, 0\} \,\mathrm{d}x\,\mathrm{d}y - V,$$

which is an increasing function with respect to λ. It is easy to verify

$$f(0) \geq \int_D \tilde{u}^{k+1} \,\mathrm{d}x\,\mathrm{d}y - V = 0$$

while for $\lambda_m = -\max(\tilde{u}^{k+1}) \leq 0$,

$$f(\lambda_m) = -V \leq 0.$$

Thus there exists a unique λ^* such that

$$\begin{cases} u^{k+1} = \max\{\tilde{u}^{k+1} + \lambda^*, 0\}, \\ \int_D u^{k+1} \,\mathrm{d}x\,\mathrm{d}y = V, \end{cases} \tag{3.53}$$

which is exactly (3.41). ∎

Rewrite (3.43) as

$$v^{k+1} = (I + \tau \partial I_K)^{-1}(\tilde{v}^{k+1}), \tag{3.54}$$

and symbolically

$$u^{k+1} = (I + \tau \partial I_K)^{-1}\tilde{u}^{k+1} := u^* + (I + \tau \partial I_K)^{-1}(\tilde{v}^{k+1}). \tag{3.55}$$

In summary, we have

$$u^{k+1} = (I + \tau \partial I_K)^{-1}(I + \tau \nabla E)^{-1}u^k. \tag{3.56}$$

Recall $A = \nabla E$, $B = \partial I_K$. The corresponding resolvent operators of A and B are denoted as $J_\tau^A := (I+\tau\nabla E)^{-1}$ and $J_\tau^B := (I+\tau\partial I_K)^{-1}$, respectively. The projection method above can be recast as

$$u^{k+1} = J_\tau^B J_\tau^A u^k. \tag{3.57}$$

Next, to obtain an approximated solution $\bar{u}_\tau(t)$ at any $t \in [0, T]$ for any time step $\tau > 0$, we use the piecewise constant interpolation from u^k such that

$$\bar{u}_\tau(t) \equiv u^k, \quad t \in [k\tau, (k+1)\tau), \tag{3.58}$$

which is equivalent to

$$\bar{u}_\tau(t) := (J_\tau^B J_\tau^A)^{[\frac{t}{\tau}]}u_0, \quad t \in [0, T]. \tag{3.59}$$

3.3.4. Convergence theorem. With all the preparations above, we apply a nonlinear version of the Trotter–Kato product formula [25] to prove the convergence for solving PVI (3.31) using the projection method.

THEOREM 3.3 (convergence of the projection method). *Let $t \in [0, T]$ and $u(t)$ given in* (3.38) *be a unique mild solution of* (3.31). *Let $\bar{u}_\tau(t)$ given in* (3.59) *be the numeric solution obtained from the projection method with time step τ. Then we have the convergence*

$$\lim_{\tau \to 0} \sup_{t \in [0,T]} \|\bar{u}_\tau(t) - u(t)\| = 0. \tag{3.60}$$

Proof. First, since $A+B = \partial(E+I_K)$ is a maximal monotone operator in u^*+X_1, $A+B$ generates a strongly continuous semigroup on $[0, +\infty)$ of contractions, denoted symbolically as $S(t) := e^{-t\partial(E+I_K)}$. For any $u_0 \in K$, the mild solution to (1.1) is given by

$$u(t) = e^{-t\partial(E+I_K)}u_0. \tag{3.61}$$

Second, recall the resolvent of A and B are $J_\tau^A = (I + \tau\nabla E)^{-1}$ and $J_\tau^B = (I + \tau\partial I_K)^{-1}$, respectively. We use the Trotter–Kato product formula [25] to prove

$$u^n(t) := \left(J_{\frac{t}{n}}^B J_{\frac{t}{n}}^A\right)^n u_0 \to u(t), \quad \text{as } n \to +\infty, \quad \text{uniformly for } t \geq 0. \tag{3.62}$$

To see this, in [25] we take $U_1 := J_{\frac{t}{n}}^A$, $U_2 := J_{\frac{t}{n}}^B$. Then by [25, Example 2.3], we know U_1 are a nice E-family with index $\gamma \geq 2$ and U_2 are a nice I_K-family with index $\gamma \geq 2$. Hence the condition (i) in [25, Theorem] holds, which gives the claim (3.62).

Finally, for the projection scheme for $t \in [0,T]$ with time step $\tau = \frac{T}{n}$, the piecewise constant interpolation in $[k\tau,(k+1)\tau)$ is given by

$$\bar{u}_\tau(t) = (J_\tau^B J_\tau^A)^{[\frac{t}{\tau}]} u_0, \quad t \in [0,T], \tag{3.63}$$

where $[a]$ is the integer part of real number a. Since $\tau[\frac{t}{\tau}] \to t$ as $\tau \to 0$, we know

$$u\left(\tau\left[\frac{t}{\tau}\right]\right) \to u(t) \tag{3.64}$$

due to continuous semigroup property. Therefore we conclude

$$\|\bar{u}_\tau(t) - u(t)\| \le \left\|(J_\tau^B J_\tau^A)^{[\frac{t}{\tau}]} u_0 - u\left(\tau\left[\frac{t}{\tau}\right]\right)\right\| + \left\|u\left(\tau\left[\frac{t}{\tau}\right]\right) - u(t)\right\| \to 0 \tag{3.65}$$

as $\tau \to 0$ uniformly in $t \in [0,T]$. ∎

4. Computations for merging and splitting of droplets. In this section, we first give an accuracy check for the numerical scheme by constructing a projected triple Gaussian capillary surface and then demonstrate two typical examples using the projection scheme proposed in section 3.1. The first example is splitting of one big droplet into two droplets when placed on an inclined groove-textured substrate. The second example is merging of two droplets in a Utah teapot, which is compared to independent dynamics of two droplets in the teapot separately.

4.1. Accuracy check with a projected triple Gaussian profile. In this subsection, to check the order of accuracy of the projection method, we construct a special example by a projected triple Gaussian function. We point out we only check the first order accuracy of the projection method for solving PVI (3.31), i.e., Steps 1–4 in section 3.1.2. In other words, when checking the first order accuracy of the projection method, we always regard the projected profile as a two-phase interface without detecting the splitting point (Step 5 in section 3.1.2).

We use the initial endpoint $b_0 = 1.3$ and a projected triple Gaussian as initial capillary surface (green line in Figure 2)

$$u_0(x) = \max\left\{2\left(e^{-(x+1)^2} + e^{-16x^2} + e^{-(x-1)^2} - e^{-(b_0+1)^2} - e^{-16b_0^2} - e^{-(b_0-1)^2}\right),\ 0\right\} \tag{4.1}$$

for $x \in [-b_0, b_0]$.

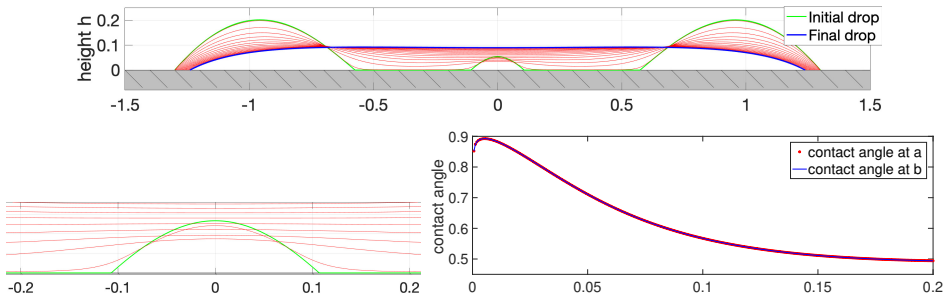

FIG. 2. *The time evolution of the capillary surface u starting from a projected triple Gaussian function* (4.1)*, shown in green line. (Top) Capillary surface at equal time intervals are shown in red line and the profile at final time $T = 0.2$ is shown in blue line. (Lower left) Zoom-in plot near $x = 0$ showing u approaches zero at an early stage. (Lower right) Dynamic contact angle tracking w.r.t. time.*

TABLE 1

Accuracy check: first order projection scheme in section 3.1.2 *versus numerically computed exact solution to* (3.8) *using time steps* $M = 1280$ *and spatial grid points* $N = 8 * M$. *Parameters:* $T = 0.2$, $\kappa = 20$, $\theta_Y = \frac{\pi}{3}$, $b_0 = 1.3$, *time step* $\Delta t = \frac{T}{M}$, M *listed on the table, moving grid size* $\Delta x = \frac{b(t)-a(t)}{N}$, $N = 8M$. *Absolute errors* e_n *for* b, u, *and* θ_{CL} *are computed by comparing with exact solutions.*

	First order scheme					
M	Error of b	Order	Error of u	Order	Error of θ_{CL}	Order
20	2.5961×10^{-3}		1.2592×10^{-3}		6.3988×10^{-3}	
40	1.3571×10^{-3}	0.936	6.3389×10^{-4}	0.990	3.0201×10^{-3}	1.083
80	6.8157×10^{-4}	0.994	3.0961×10^{-4}	1.034	1.4511×10^{-3}	1.057
160	3.2538×10^{-4}	1.067	1.4555×10^{-4}	1.089	6.7734×10^{-4}	1.099
320	1.4151×10^{-4}	1.201	6.2874×10^{-5}	1.211	2.8999×10^{-4}	1.224

The physical parameters in (3.8) for the first order scheme in section 3.1.2 are

$$\kappa = 20, \quad \beta = 2, \quad \sigma = -\cos\frac{\pi}{3} = -\frac{1}{2}, \quad w(x) \equiv 0, \tag{4.2}$$

where $\theta_Y = \frac{\pi}{3}$ is the Young's angle. Choose a final time $T = 0.2$. We numerically compute an exact solution $b(T) = 1.238369607448268$, $\theta_{\mathrm{CL}}(T) = 0.493880485215342$ with uniform time steps $\Delta t = \frac{T}{M}$, $M = 1280$ and uniform $N = 8 * M$ moving grid points in $[a(t), b(t)]$.

We show the accuracy check for the first order scheme in section 3.1.2 in Table 1. We use the same physical parameters and initial data in the first order schemes. For several M_n listed in the tables, we take the time step as $\Delta t = \frac{T}{M_n}$ and moving grid size $\Delta x = \frac{b(t)-a(t)}{N_n}$ with $N_n = 8M_n$. The absolute error $e_n = |b^{M_n} - b(T)|$ (resp., $e_n = |\theta_{\mathrm{CL}}^{M_n} - \theta_{\mathrm{CL}}(T)|$) between numeric solutions and the numerically computed exact contact point $b(T)$ (resp., exact contact angle $\theta_{\mathrm{CL}}(T)$) are listed in the second column (resp., sixth column) of Table 1. The maximal norm error $e_n = \|u^{M_n} - u(\cdot, T)\|_{\ell^\infty}$ between numeric solutions and the numerically computed exact capillary profile u is listed in the fourth column of Table 1. The corresponding order of accuracy $\alpha = \frac{\ln(e_n/e_{n+1})}{\ln(M_{n+1}/M_n)}$ is listed in the last column of the tables. For $M = 320$, the time evolution of the capillary surface is shown in Figure 2 (top) with red lines at equal time intervals. A zoom-in plot showing the capillary surface for the small bump profile at $x = 0$ approaches zero at the early stage of the evolution. We also track the time history of two contact angles up to the final time $T = 0.2$; see Figure 2 (bottom).

4.2. Computations. Now we use the projection scheme in section 3.1 to simulate two challenging examples including the splitting and merging of droplets on different impermeable substrates.

4.2.1. Example 1: Splitting of one droplet on an inclined groove-textured substrate. We take a typical groove-textured substrate

$$w(x) = A(\sin(kx) + \cos(2kx))^2, \; A = 0.1, \; k = 2.5. \tag{4.3}$$

This is an impermeable obstacle where phase transitions happen when the droplet touches the obstacle. Thus at the touching point, after one detects the phase transition, one droplet will split into two independent droplets with their own PVI (3.4).

To demonstrate those phenomena, we take the physical parameters as $\kappa = 1$, $\beta = 0.1$, effective inclined angle $\theta_0 = 0.3$, and initial droplet as

$$h(x,0) = 0.1(x - a(0))(b(0) - x) + w(a(0)) + \frac{[w(b(0)) - w(a(0))](x - a(0))}{b(0) - a(0)} \tag{4.4}$$

with initial endpoints $a(0) = -2.1$, $b(0) = 3.1$ as shown in Figure 3 using a green line. The corresponding effective Bond number can be calculated as in Remark 1 with effective inclined angle $\theta_0 = 0.3$, Bo $= 0.5712$. We take final time as $T = 1$ with time step $\Delta t = 0.005$ and use $N = 200$ moving grids uniformly in $(a(t), b(t))$ in the projection scheme. With relative adhesion coefficient $\sigma = -0.52$, in Figure 3, we show the dynamics of the droplet on groove-textured surface $w(x)$ in (4.3) at equal time intervals using thin red lines. The splitting time detected is $T_s = 0.035$ with threshold $\varepsilon = 0.075$ and the two generated droplets keep moving independently until the final time $T = 1$ with the final profiles shown in solid blue lines.

4.2.2. Example 2: Two droplets merged together in a Utah teapot. We use a Utah teapot, which is well-known in computer graphics history, as a typical inclined groove-textured substrate to demonstrate the merging of two droplets. The Utah teapot can be constructed by several cubic Bézier curves [4] connecting following 10 points x_i, y_i, $i = 1, \ldots, 10$, as listed in Table 2. For the bottom of the teapot, we use (x_i, y_i) for $i = 1, \ldots, 4$ and (x_i, y_i) for $i = 4, \ldots, 7$. For the mouth of the teapot,

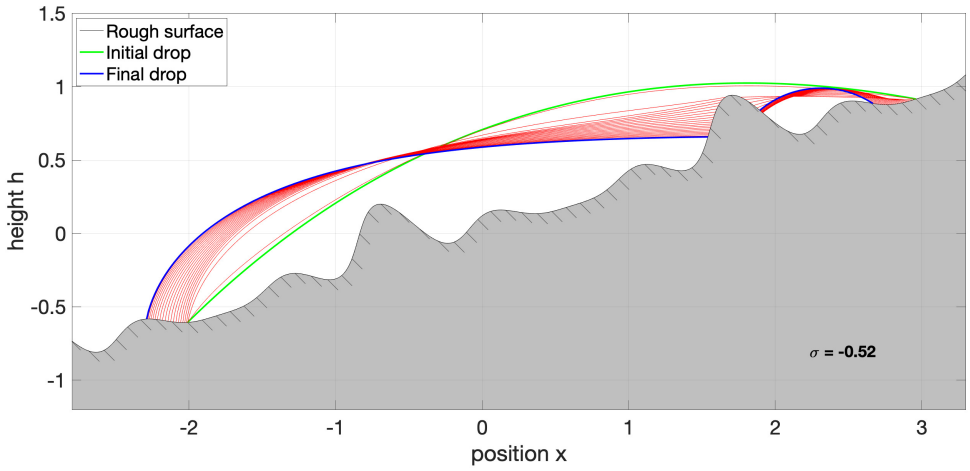

FIG. 3. *Evolution and splitting of one droplet into two droplets on an inclined groove-textured surface using the projection scheme in section* 3.1. *Parameters:* $\kappa = 1$, $\beta = 0.1$, *number of moving grids* $N = 200$, *time step* $\Delta t = 0.005$, *final time* $T = 1$, *splitting threshold* $\varepsilon = 0.075$, *initial drop profile (green line)* $h(x,t)$ *in* (4.4) *with initial endpoints* $a(0) = -2.1, b(0) = 3.1$, *Bond number* Bo $= 0.5712$., *relative adhesion coefficient* $\sigma = -0.95$, *and the inclined substrate with effective angle* $\theta_0 = 0.3$ *and* (4.3). *The evolution is shown using red lines at equal time intervals, and the final profiles of two new droplets are shown in a blue line.*

TABLE 2
Ten points used in Bézier curve fitting of geometry of a Utah teapot.

i	1	2	3	4	5	6	7	8	9	10
x_i	-2	$-\frac{4}{3}$	$-\frac{2}{3}$	0	$\frac{2}{3}$	$\frac{4}{3}$	2	2.655	2.846	4
y_i	0.78	0	0	0	0	0	0.78	1.142	2.146	2.5

we use (x_i, y_i) for $i = 7, \ldots, 10$. Assume the inclined groove-textured substrate is expressed by a parametric curve $(x(\ell), y(\ell))$. Let $\ell(x)$ be the inverse function of $x(\ell)$, then $w(x) = y(\ell(x))$ in (3.4).

Now we take the physical parameters as $\kappa = 20$, $\beta = 1$ and the relative adhesion coefficient as $\sigma = -0.78$. Assume the initial Droplet 1 is

$$h(x,0) = 4.5(x - a(0))(b(0) - x) + w(a(0)) + \frac{[w(b(0)) - w(a(0))](x - a(0))}{b(0) - a(0)} \tag{4.5}$$

with initial endpoints $a(0) = 1.9, b(0) = 2.2$, as shown in Figure 4 with a magenta double-dotted line. Assume the initial Droplet 2 is

$$h(x,0) = 7.8(x - a(0))(b(0) - x) + w(a(0)) + \frac{[w(b(0)) - w(a(0))](x - a(0))}{b(0) - a(0)} \tag{4.6}$$

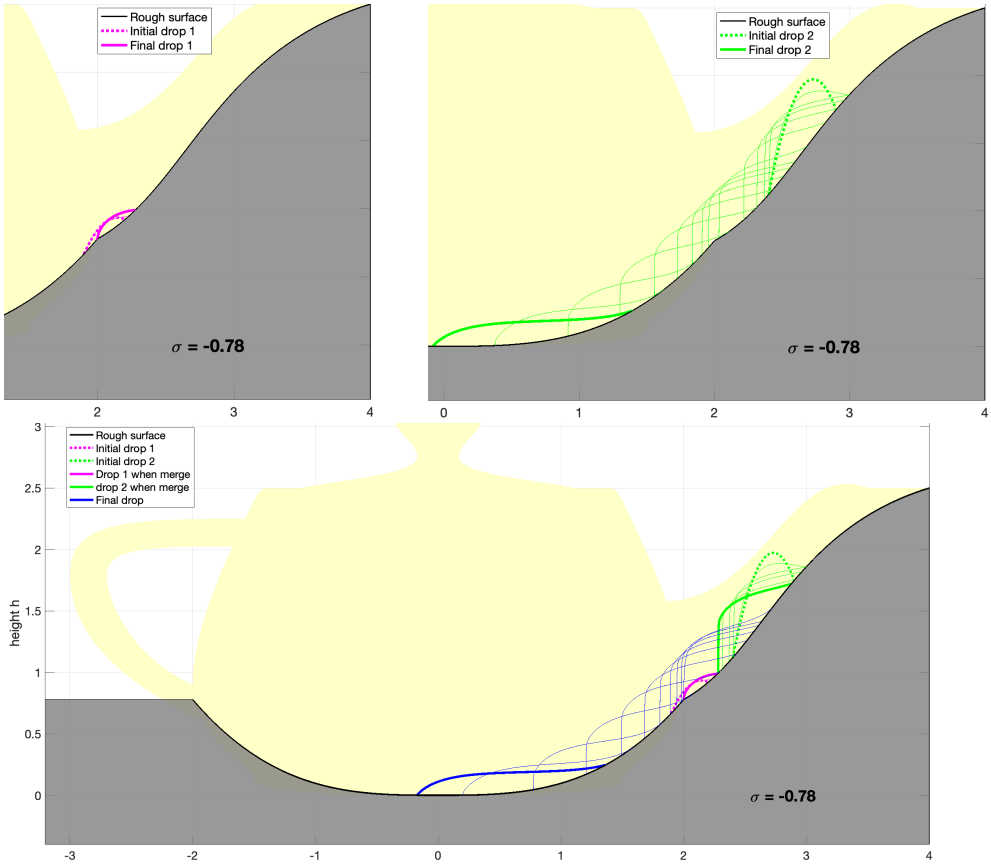

FIG. 4. *Evolution of two partially wetting droplets in the Utah teapot at equal time intervals using the scheme in section* 3.1. *Parameters: number of moving grids in drop* $N = 1000$, *time step* $\Delta t = 0.05$, *final time* $T = 12$, $\kappa = 20$, $\beta = 1$, *relative adhesion coefficient* $\sigma = -0.78$, *merging threshold* $\varepsilon = 0.01$, *Bond number* $\mathrm{Bo} = 0.0832$ *for Droplet* 1 *and* $\mathrm{Bo} = 0.7861$ *for Droplet* 2, *initial Droplet* 1 *profile (magenta double-dotted line) given in* (4.5) *with* $a(0) = 1.9, b(0) = 2.2$ *and initial Droplet* 2 *profile (green double-dotted line) given in* (4.6) *with* $a(0) = 2.4, b(0) = 2.9$. *(Upper left) Droplet* 1 *with slow capillary rise. (Upper right) Droplet* 2 *moves down fast due to gravitational effect. (Bottom) Dynamics of two droplets: merge together and then move down as a new big droplet with final profile shown in solid blue lines.*

with initial endpoints $a(0) = 2.4, b(0) = 2.9$ as shown in Figure 4 with a green double-dotted line. The corresponding effective Bond number can be calculated according to Remark 1 with effective inclined angle $\theta_0 = 0.226\pi$, Bo $= 0.0832$ for Droplet 1, and Bo $= 0.7861$ for Droplet 2. In the numeric scheme, we use $N = 1000$ moving grids uniformly in $(a(t), b(t))$ and the merging threshold $\varepsilon = 0.01$. We take the same final time $T = 12$ with time step $\Delta t = 0.05$. Without merging, the dynamics at equal time intervals of Droplet 1 and Droplet 2 are shown separately as comparisons in Figure 4 (top) with the final profile at $T = 12$ using a solid magenta line for Droplet 1 and a solid green line for Droplet 2. The small magenta Droplet 1 (top left) shows slow capillary rise, while the large green Droplet 2 (top right) moves down fast due to the gravitational effect. However, with the same parameters and same initial profiles (double-dotted lines), the dynamics at equal time intervals for the two droplets placed together in the Utah teapot are shown in Figure 4 (bottom). The two droplets will merge together at $T = 3$ with the solid magenta/green lines for Droplet 1/Droplet 2 and then they continue to move down as a new big droplet as shown in thin blue lines. The final profile of the new big droplet at $T = 12$ is shown in a solid blue line.

Acknowledgment. The authors would like to thank Prof. Tom Witelski for some helpful suggestions.

REFERENCES

[1] L. Almeida, A. Chambolle, and M. Novaga, *Mean curvature flow with obstacles*, Ann. Inst. H. Poincaré Anal. Non Linéaire, 29 (2012), pp. 667–681, https://doi.org/10.1016/j.anihpc.2012.03.002.

[2] F. Almgren, J. E. Taylor, and L. Wang, *Curvature-driven flows: A variational approach*, SIAM J. Control Optim., 31 (1993), pp. 387–438, https://doi.org/10.1137/0331020.

[3] J. W. Barrett, H. Garcke, and R. Nürnberg, *Parametric finite element approximations of curvature-driven interface evolutions*, in Geometric Partial Differential Equations Handb. Numer. Anal. 21, Elsevier, Amsterdam, 2020, pp. 275–423.

[4] W. Böhm, G. Farin, and J. Kahmann, *A survey of curve and surface methods in CAGD*, Comput. Aided Geom. Design, 1 (1984), pp. 1–60.

[5] H. Brezis, *Opérateurs maximaux monotones: et semi-groupes de contractions dans les espaces de hilbert*, North-Holland, Amsterdam, 1973.

[6] L. A. Caffarelli, K.-A. Lee, and A. Mellet, *Homogenization and flame propagation in periodic excitable media: The asymptotic speed of propagation*, Comm. Pure Appl. Math., 59 (2006), pp. 501–525.

[7] L. A. Caffarelli and A. Mellet, *Capillary drops: Contact angle hysteresis and sticking drops*, Calc. Var. Partial Differential Equations, 29 (2007), pp. 141–160, https://doi.org/10.1007/s00526-006-0036-y.

[8] L. A. Caffarelli and A. Mellet, *Capillary drops on an inhomogeneous surface*, in Perspectives in Nonlinear Partial Differential Equations, Contemp. Math. 446, AMS, Providence, RI, 2007, pp. 175–201, https://doi.org/10.1090/conm/446/08631.

[9] X. Chen, X.-P. Wang, and X. Xu, *Effective contact angle for rough boundary*, Phys. D, 242 (2013), pp. 54–64, https://doi.org/10.1016/j.physd.2012.08.018.

[10] A. J. Chorin, *On the convergence of discrete approximations to the Navier–Stokes equations*, Math. Comp., 23 (1969), pp. 341–353.

[11] P. G. de Gennes, *Wetting: statics and dynamics*, Rev. Modern Phys., 57 (1985), pp. 827–863, https://doi.org/10.1103/RevModPhys.57.827.

[12] P.-G. De Gennes, F. Brochard-Wyart, and D. Quéré, *Capillarity and Wetting Phenomena: Drops, Bubbles, Pearls, Waves*, Springer, New York, 2013.

[13] E. Dussan, *On the ability of drops or bubbles to stick to non-horizontal surfaces of solids. Part 2. Small rops or bubbles having contact angles of arbitrary size*, J. Fluid Mec., 151 (1985), pp. 1–20.

[14] W. E and X.-P. Wang, *Numerical methods for the Landau–Lifshitz equation*, SIAM J. Numer. Anal., 38 (2001), pp. 1647–1665.

[15] S. Esedoglu and F. Otto, *Threshold dynamics for networks with arbitrary surface tensions*, Comm. Pure Appl. Math., 68 (2015), pp. 808–864, https://doi.org/10.1002/cpa.21527.
[16] S. Esedoglu, R. Tsai, and S. Ruuth, *Threshold dynamics for high order geometric motions*, Interfaces Free Bound., 10 (2008), pp. 263–282, https://doi.org/10.4171/IFB/189.
[17] W. M. Feldman and I. C. Kim, *Dynamic stability of equilibrium capillary drops*, Arch. Ration. Mech. Anal., 211 (2014), pp. 819–878, https://doi.org/10.1007/s00205-013-0698-5.
[18] W. M. Feldman and I. C. Kim, *Liquid drops on a rough surface*, Comm. Pure Appl. Math., 71 (2018), pp. 2429–2499, https://doi.org/10.1002/cpa.21793.
[19] Y. Gao and J.-G. Liu, *Gradient flow formulation and second order numerical method for motion by mean curvature and contact line dynamics on rough surface*, Interfaces Free Bound., 23 (2021), pp. 103–158.
[20] Y. Gao and J.-G. Liu, *Surfactant-dependent contact line dynamics and droplet adhesion on textured substrates: Derivations and computations*, Phys. D, 428 (2021), 133067.
[21] R. Glowinski, J.-L. Lions, and R. Trémolières, *Numerical Analysis of Variational Inequalities*, Stud. Math. Appl. 8, North-Holland, Amsterdam, 1981.
[22] H. Goldstein, C. Poole, and J. Safko, *Classical Mechanics, 3rd ed.,* Addison-Wesley, Reading, MA, 2002.
[23] N. Grunewald and I. Kim, *A variational approach to a quasi-static droplet model*, Calc. Var. Partial Differential Equations, 41 (2011), pp. 1–19, https://doi.org/10.1007/s00526-010-0351-1.
[24] W. Jiang, W. Bao, C. V. Thompson, and D. J. Srolovitz, *Phase field approach for simulating solid-state dewetting problems*, Acta Materialia, 60 (2012), pp. 5578–5592, https://doi.org/10.1016/j.actamat.2012.07.002.
[25] T. Kato and K. Masuda, *Trotter's product formula for nonlinear semigroups generated by the subdifferentials of convex functionals*, J. Math. Soc. Japan, 30 (1978), pp. 169–178, https://doi.org/10.2969/jmsj/03010169.
[26] I. Kim and A. Mellet, *Liquid drops sliding down an inclined plane*, Trans. Amer. Math. Soc., 366 (2014), pp. 6119–6150, https://doi.org/10.1090/S0002-9947-2014-06236-3.
[27] D. Kinderlehrer and G. Stampacchia, *An Introduction to Variational Inequalities and Their Applications*, SIAM, Philadelphia, 2000, https://doi.org/10.1137/1.9780898719451.
[28] W. P. Klingenberg, *Riemannian Geometry*, De Gruyter, Berlin, 2011, https://doi.org/doi:10.1515/9783110905120.
[29] Y. Komura, *Nonlinear semi-groups in Hilbert space*, J. Math. Soc. Japan, 19 (1967), pp. 493–507.
[30] S. Leung and H. Zhao, *A grid based particle method for moving interface problems*, J. Comput. Phys., 228 (2009), pp. 2993–3024, https://doi.org/10.1016/j.jcp.2009.01.005.
[31] Z. Li, M.-C. Lai, G. He, and H. Zhao, *An augmented method for free boundary problems with moving contact lines*, Comput. & Fluids, 39 (2010), pp. 1033–1040.
[32] S. Luckhaus and T. Sturzenhecker, *Implicit time discretization for the mean curvature flow equation*, Calc. Var. Partial Differential Equations, 3 (1995), pp. 253–271.
[33] G. Mercier and M. Novaga, *Mean curvature flow with obstacles: Existence, uniqueness and regularity of solutions*, Interfaces Free Bound., 17 (2015), pp. 399–427.
[34] L. W. Morland, *A fixed domain method for diffusion with a moving boundary*, J. Engrg. Math., 16 (1982), pp. 259–269, https://doi.org/10.1007/BF00042720.
[35] L. Mugnai, C. Seis, and E. Spadaro, *Global solutions to the volume-preserving mean-curvature flow*, Calc. Var. Partial Differential Equations, 55 (2016).
[36] T. Qian, X.-P. Wang, and P. Sheng, *A variational approach to moving contact line hydrodynamics*, J. Fluid Mech., 564 (2006), pp. 333–360, https://doi.org/10.1017/S0022112006001935.
[37] W. Ren and W. E, *Boundary conditions for the moving contact line problem*, Phys. Fluids, 19 (2007), 022101.
[38] E. Schäffer and P.-z. Wong, *Dynamics of contact line pinning in capillary rise and fall*, Phys. Rev. Lett., 80 (1998), 3069.
[39] R. Scholz, *Numerical solution of the obstacle problem by the penalty method*, Computing, 32 (1984), pp. 297–306, https://doi.org/10.1007/BF02243774.
[40] R. Temam, *Quelques méthodes de décomposition en analyse numérique*, Actes Congrés Intern. Math. (1970), pp. 311–319.
[41] G. Tran, H. Schaeffer, W. M. Feldman, and S. J. Osher, *An L^1 penalty method for general obstacle problems*, SIAM J. Appl. Math., 75 (2015), pp. 1424–1444, https://doi.org/10.1137/140963303.
[42] D. Wang, X.-P. Wang, and X. Xu, *An improved threshold dynamics method for wetting dynamics*, J. Comput. Phys., 392 (2019), pp. 291–310, https://doi.org/10.1016/j.jcp.2019.04.037.

[43] Y. Wang, W. Jiang, W. Bao, and D. J. Srolovitz, *Sharp interface model for solid-state dewetting problems with weakly anisotropic surface energies*, Phys. Rev. B, 91 (2015), 045303, https://doi.org/10.1103/PhysRevB.91.045303.
[44] S. Xu and W. Ren, *Reinitialization of the level-set function in 3D simulation of moving contact lines*, Commun. Comput. Phys., 20 (2016), pp. 1163–1182.
[45] X. Xu, D. Wang, and X.-P. Wang, *An efficient threshold dynamics method for wetting on rough surfaces*, J. Comput. Phys., 330 (2017), pp. 510–528.
[46] T. Young, III. *An essay on the cohesion of fluids*, Philos. Trans. Roy. Soc. London, (1805), pp. 65–87.
[47] H.-K. Zhao, T. Chan, B. Merriman, and S. Osher, *A variational level set approach to multiphase motion*, J. Comput. Phys. 127 (1996), pp. 179–195, https://doi.org/10.1006/jcph.1996.0167.
[48] D. Zosso, B. Osting, M. Xia, and S. J. Osher, *An efficient primal-dual method for the obstacle problem*, J. Sci. Comput., 73 (2017), pp. 416–437, https://doi.org/10.1007/s10915-017-0420-0.